RSC Advances

PAPER

View Article Online
View Journal | View Issue

Cite this: *RSC Adv.*, 2026, **16**, 21079

Discovery of thieno[2,3-*d*]pyrimidine-based dual Aurora B/VEGFR-2 inhibitors with potent anticancer activity: molecular docking, mechanistic studies, and *in vivo* validation in a breast cancer model

Hamed W. El-Shafey, [a] Abdelrahman Hamdi, *[a] Mohamed R. Elnagar, [bc] Sahar M. Gebril, [d] Abdullah Haikal, [e] Adel S. El-Azab, [f] Simone Brogi, [g] Ibrahim A. Al-Suwaidan [f] and Alaa A.-M. Abdel-Aziz [f]

Breast cancer continues to be the most common malignancy in women and a major contributor of cancer-related mortality, emphasizing the need for novel therapeutic agents. A novel series of thienopyrimidine analogues were designed as dual Aurora B and VEGFR-2 inhibitors. Among them, compound **M1** showed the highest potency, displaying strong cytotoxicity against breast MCF-7 (IC_{50} = 3.61 μM) and MDA-MB-231 (IC_{50} = 5.37 μM) cells, comparable to Doxorubicin and superior to Sorafenib. The *in vitro* enzyme inhibition assays revealed that **M1** inhibited Aurora B and VEGFR-2 with IC_{50} values of 0.037 and 0.220 μM, respectively. In MDA-MB-231 cells, **M1** induced G1-phase arrest and enhanced apoptosis, reducing viable cells to 54.6% and increasing total apoptotic cells to 21.3%. *In vivo*, **M1** reduced tumor volume by 58.6% in a DMBA-induced breast cancer model, comparable to Doxorubicin (64.8%) but with lower systemic toxicity. Histopathology and caspase-3 staining confirmed reduced malignancy and restored apoptotic activity. Molecular docking and dynamics suggested stable binding of **M1** within Aurora B and VEGFR-2 active sites.

Received 4th December 2025
Accepted 14th April 2026

DOI: 10.1039/d5ra09370h

rsc.li/rsc-advances

1 Introduction

Breast cancer continues to be the most frequently diagnosed malignancy worldwide and the foremost cause of cancer-related death in women.[1] Recent analyses from the International Agency for Research on Cancer report that around 2.3 million new cases and 670 000 deaths occurred worldwide in 2022, with the incidence rates for breast cancer rising by 1–5% per year in approximately half of monitored countries. Projections indicate that if current trends persist, these numbers could increase to 3.2 million new diagnoses and around 1 million deaths each year by 2050, disproportionately impacting countries with lower Human Development Index.[2]

Triple-negative breast cancer (TNBC) represents roughly 10–15% of all breast cancer cases and is characterized by the absence of estrogen and progesterone receptors and a lack of HER2 protein overexpression.[3,4] TNBC is clinically aggressive, tends to present in younger patients and in those with BRCA1 mutations, and displays a poor prognosis due to rapid progression, higher recurrence rates, and limited therapeutic options, primarily reliance on chemotherapy rather than targeted endocrine or HER2 therapies.[5] The aggressive nature of TNBC and the absence of targeted treatment options underscore the urgent need for novel therapeutic candidates in this subtype.[6]

Aurora B kinase is a serine/threonine kinase that regulates multiple mitotic processes, including chromosome alignment, segregation, and cytokinesis.[6,7] Aurora B overexpression or dysregulation is often observed in human cancers, including breast cancer, and is frequently associated with aggressive disease and poorer clinical outcomes.[8,9] Notably, the expression of Aurora B is particularly elevated in TNBC, where its abnormal ratio to its regulator, INCENP, leads to mitotic defects and resistance to conventional therapies.[10,11] Targeted inhibition of Aurora B suppresses tumor cell proliferation in preclinical

[a]*Department of Pharmaceutical Organic Chemistry, Faculty of Pharmacy, Mansoura University, Mansoura 35516, Egypt. E-mail: abdelrahmanhamdi2012@mans.edu.eg*
[b]*Department of Pharmacology and Toxicology, Faculty of Pharmacy, Al-Azhar University, Cairo 11823, Egypt*
[c]*Department of Pharmacology, College of Pharmacy, The Islamic University, Najaf 54001, Iraq*
[d]*Department of Histology and Cell Biology, Faculty of Medicine, Sohag University, Sohag 82524, Egypt*
[e]*Department of Pharmacognosy, Faculty of Pharmacy, Mansoura University, Mansoura, 35516, Egypt*
[f]*Department of Pharmaceutical Chemistry, College of Pharmacy, King Saud University, P. O. Box 2457, Riyadh 11451, Saudi Arabia*
[g]*Department of Pharmacy, University of Pisa, Via Bonanno 6, 56126 Pisa, Italy*

models and enhances the effects of cytotoxic agents and radiotherapy, making it a promising candidate for anti-breast cancer therapeutics, particularly for patients with TNBC who urgently need new treatment paradigms.[10,12]

Several Aurora B selective inhibitors have been developed. Some of them entered clinical trials for cancer therapy,[13] such as Barasertib (AZD115214, **I**),[14] SNS-314 (**II**),[15] Ilorasertib (APT-348, **III**),[16] BPR1K653 (**IV**),[17] and SP-96 (**V**)[18] (Fig. 1). A recent study revealed that Barasertib (**I**) markedly reduced colony formation in TNBC cell lines, and its combination with radiotherapy at IC_{50} concentrations resulted in an even greater inhibitory effect than single-agent treatment.

Angiogenesis inhibition has emerged as a beneficial therapeutic approach for combating cancer, particularly due to the heightened vascularization observed in malignant tumors, which supports the metabolic demands and rapid proliferation of tumor cells.[19] This process is largely mediated by the overexpression of receptor tyrosine kinases (RTKs), such as angiokinases, with vascular endothelial growth factor receptors (VEGFRs) playing a critical role in breast cancer. Among these, VEGFR-2 is especially crucial, as both VEGF and VEGFR-2 are significantly overexpressed in breast tumors, driving angiogenesis that underpins tumor growth, metastasis, and poor clinical outcomes.[20,21] Notably, in TNBC, VEGFR-2 assumes an expanded role by facilitating the maintenance of cancer stem cells and promoting chemoresistance through the activation of signaling pathways such as JAK2/STAT3, thereby supporting tumor self-renewal and further progression.[22] Consequently, the central involvement of VEGFR-2 in angiogenesis, cancer stem cell biology, and therapeutic resistance underscores its potential as a dual-action molecular target for the development of advanced anti-breast cancer agents, particularly for addressing the therapeutic challenges associated with TNBC (Fig. 2). Numerous inhibitors of VEGFR-2 kinase have been designed and approved or clinically tested as potent anti-cancer candidates such as Sorafenib (**VI**), Regorafenib (**VII**), Sunitinib (**VIII**), Linifanib (**IX**), Lenvatinib (**X**) and Tivozanib (**XI**).

The thieno[2,3-*d*]pyrimidine nucleus has emerged as a privileged heterocyclic scaffold in medicinal chemistry, widely recognized for its drug-like properties and structural analogy to purine, the fundamental nucleotides building block.[23,24] Because of its isoelectronic relationship with adenine, this

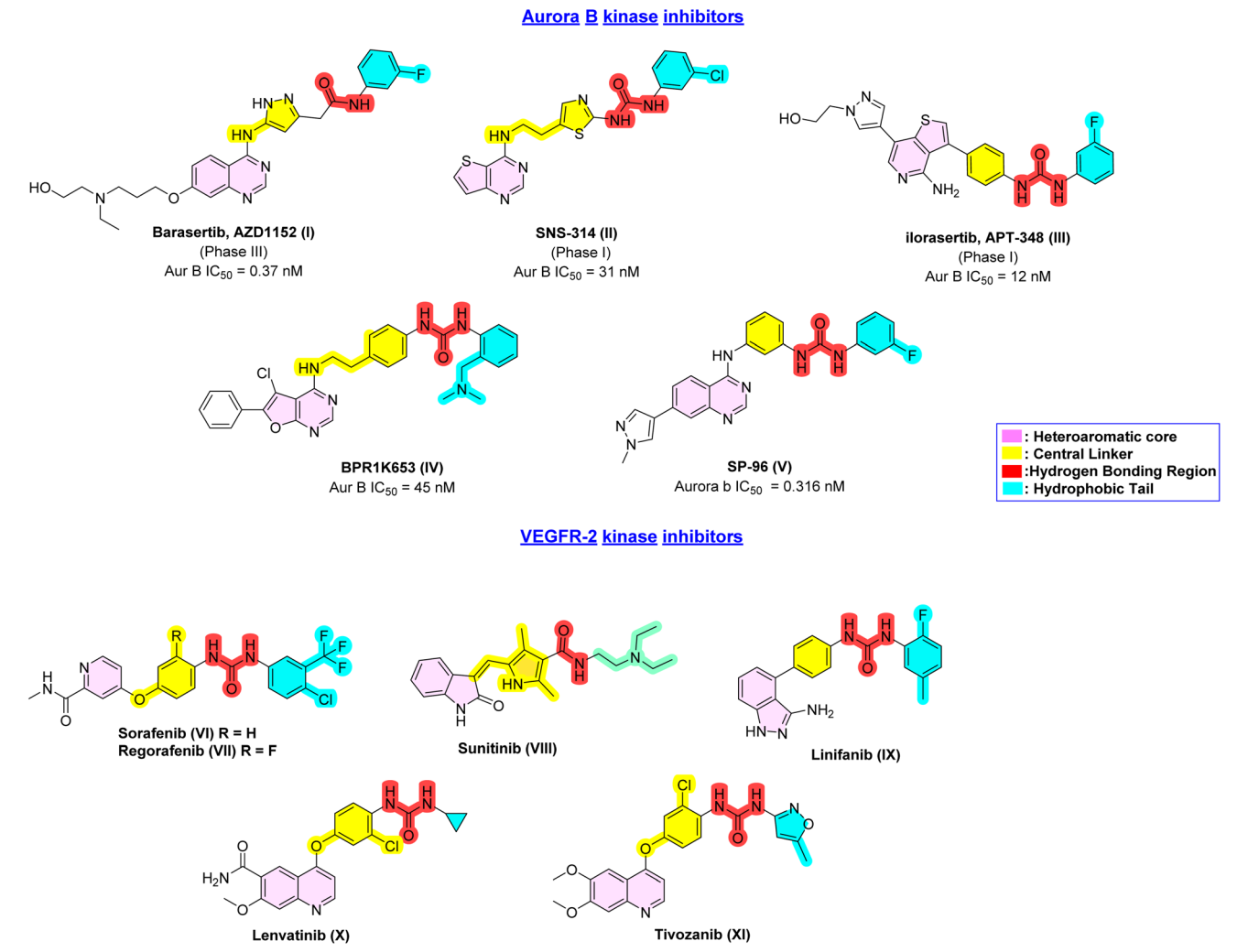

Fig. 1 Key structural elements of selected Aurora B and VEGFR-2 inhibitors.

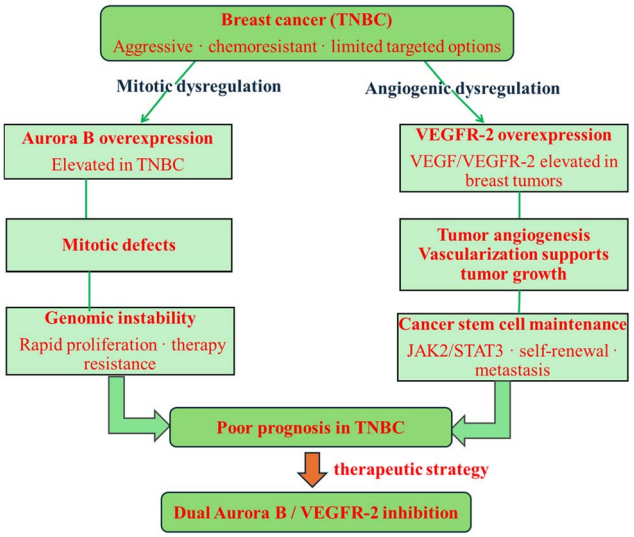

Fig. 2 Simple schematic illustrating the proposed dual mechanism (Aurora B-mediated cell cycle arrest and VEGFR-2 related signaling inhibition).

scaffold demonstrates excellent compatibility with ATP-binding sites of kinases, making it a valuable chemotype in anticancer drug discovery.[25,26] Numerous studies have documented the cytotoxic and antiproliferative activities of thieno[2,3-*d*]pyrimidine derivatives, with mechanisms involving the inhibition of key oncogenic kinases, such as Aurora B and VEGFR-2.[27–30] As an Aurora B inhibitor, a representative thienopyrimidine derivative (compound **XII**) (Fig. 3) exhibited potent activity with an IC_{50} value of 0.2 nM, underscoring the suitability of this scaffold for targeting mitotic regulation.[28] Similarly, several thienopyrimidine-based compounds have been developed as VEGFR-2 inhibitors, including compound **XIII**, which demonstrated inhibitory activities with IC_{50} values of 3.9 nM,[29] and compound **XIV** that inhibits VEGFR-2 phosphorylation.[31] Collectively, these findings highlight the versatility of the thieno[2,3-*d*]pyrimidine core as a dual-targeting pharmacophore, offering a promising foundation for the development of novel anticancer agents capable of simultaneously impairing angiogenesis and mitotic progression.

2 Results and discussion

2.1. Rational design

The rational design of our dual Aurora B and VEGFR-2 inhibitors was based on a comprehensive analysis of structure–activity relationships (SAR) and co-crystallographic data of the prototypical Aurora B inhibitor Barasertib[25,32] and VEGFR-2 inhibitor Sorafenib.[33–37] These investigations revealed that both kinase targets accommodate inhibitors with four convergent pharmacophoric features. These compromise (i) a planar heteroaromatic core, represented by scaffolds such as indole, quinazoline, thienopyrimidine, quinoline, or furanopyrimidine, serves as the principal hinge-binding element, facilitating critical anchoring within the ATP-binding site. The core structure is characterized by the presence of a hydrogen bond acceptor, typically a nitrogen atom, enabling interaction with A173 in Aurora B and C919 in VEGFR-2. (ii) A spatial linker segment that strategically bridges the hinge-binding region to the DFG-motif domain, orchestrating optimal molecular orientation for effective inhibition. This segment is often realized as either a central aryl linker or a five-membered heterocyclic ring. (iii) A pharmacophoric donor–acceptor functional group that interfaces with the DFG-motif, exemplified by amide or urea structures, enables pivotal hydrogen bonding with key residues: E885 and D1046 in VEGFR-2, and K122 and Q145 in Aurora B kinases. (iv) A hydrophobic tail moiety that extends into the back allosteric pocket of both enzymes, maximizing compound potency *via* hydrophobic interactions with nonpolar residues, and contributing to the selectivity and efficacy of advanced inhibitor scaffolds.

Building on these pharmacophoric principles, our scaffold design incorporates a thieno[2,3-*d*]pyrimidine backbone as the hinge-binding heteroaromatic core. To bridge this motif with the DFG-engaging pharmacophore, we introduced a 1,3,4-thiadiazole spacer, a privileged motif previously validated as an effective linker in VEGFR-2 inhibitors as in compound **XIV**[31] and as reported in our previous work.[34,38] A urea functional group was introduced downstream of the spacer to form donor–acceptor interactions with key DFG-domain residues in both Aurora B and VEGFR-2. Finally, a hydrophobic substituent was appended to the urea unit to project into the conserved back

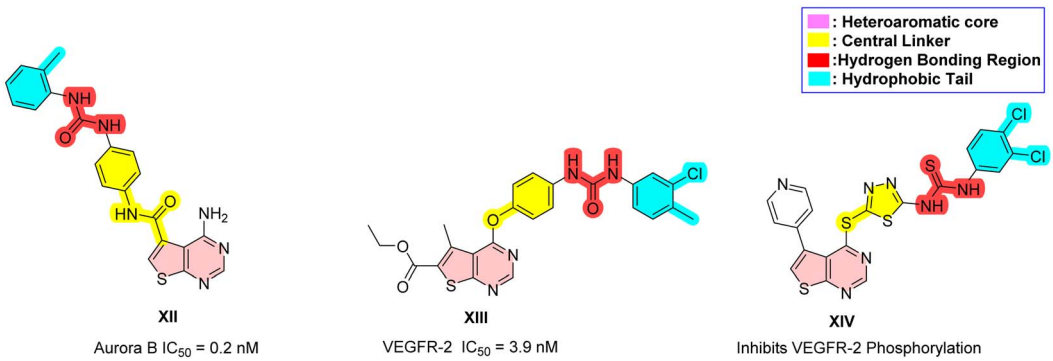

Fig. 3 Representative examples of thieno[2,3-*d*]pyrimidine as Aurora B and VEGFR-2 inhibitors.

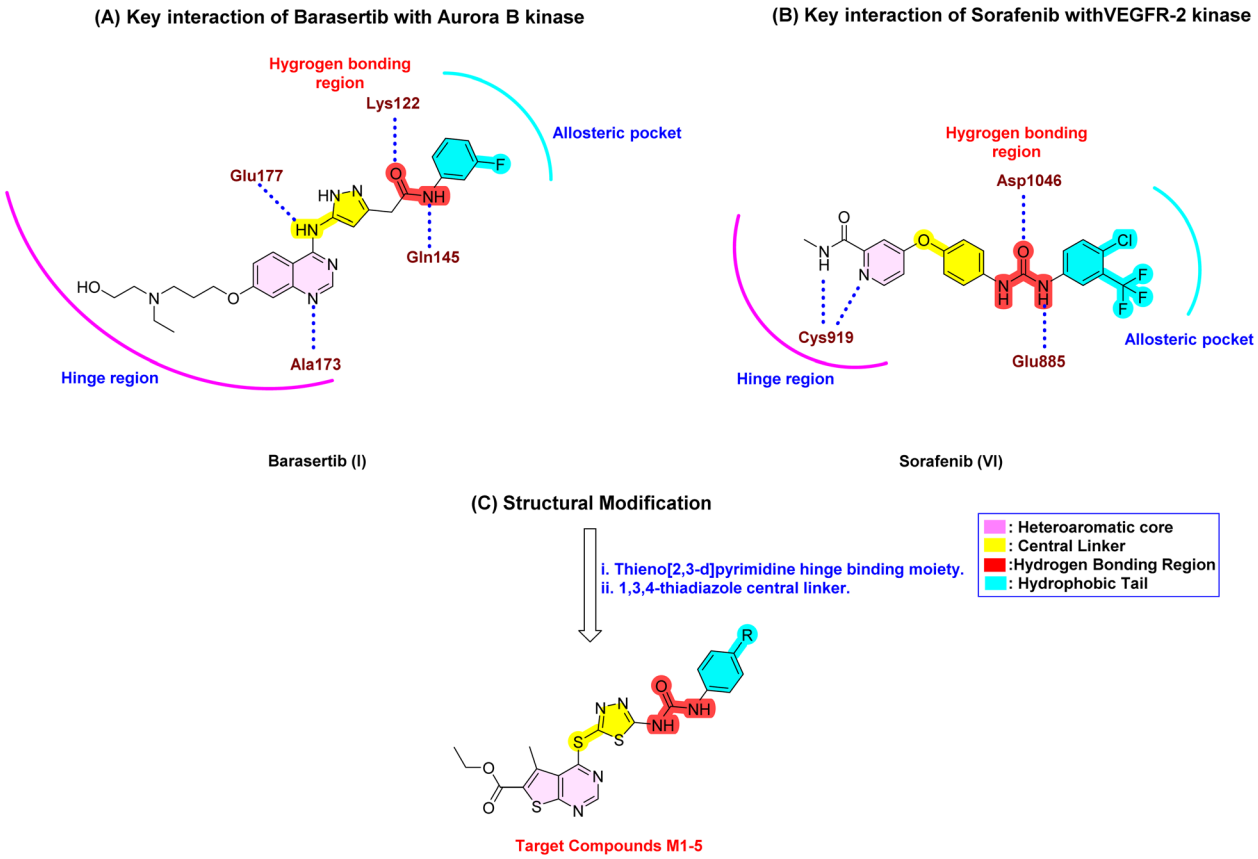

Fig. 4 Key interaction between the co-crystallized structure of (A) Barasertib and Aurora B (PDB: 4C2V),[25] (B) Sorafenib and VEGFR-2 (PDB code: 4ASD),[37] and (C) structure of the target compounds **M1–M5** and rational design.

hydrophobic pocket, maximizing π–π and hydrophobic contacts while enhancing dual-target potency (Fig. 4).

2.2. Chemistry

The synthesis of the target thienopyrimidine derivatives **M1–M5** is illustrated in Schemes 1 and 2. First, the key intermediates **3a–e** were prepared by treating thiosemicarbazide (**1**) with carbon disulfide, resulting in the formation of 5-amino-1,3,4-thiadiazole-2-thiol (**2**). The subsequent condensation of compound **2** with various substituted phenyl isocyanates afforded intermediates **3a–e** in high yields and purity, as shown in Scheme 1.[31,34,38]

As depicted in Scheme 2, ethyl 5-amino-4-cyano-3-methylthiophene-2-carboxylate (**6**) was obtained through the Gewald reaction using ethyl acetoacetate, sulfur, and malononitrile in the presence of triethylamine.[39] Compound **6** was cyclized under reflux in formic acid at 120 °C to afford ethyl 5-methyl-4-oxo-3,4-dihydrothieno[2,3-*d*]pyrimidine-6-carboxylate (**7**). The carbonyl group of **7** was subsequently chlorinated with phosphoryl chloride to yield ethyl 4-chloro-5-methylthieno[2,3-*d*]pyrimidine-6-carboxylate (**8**).[40] Finally, the nucleophilic aromatic substitution of the chlorine in compound **8** with the thiol group of intermediates **3a–e,** using potassium carbonate in DMF, afforded the target thienopyrimidine products **M1–M5** in excellent yields.

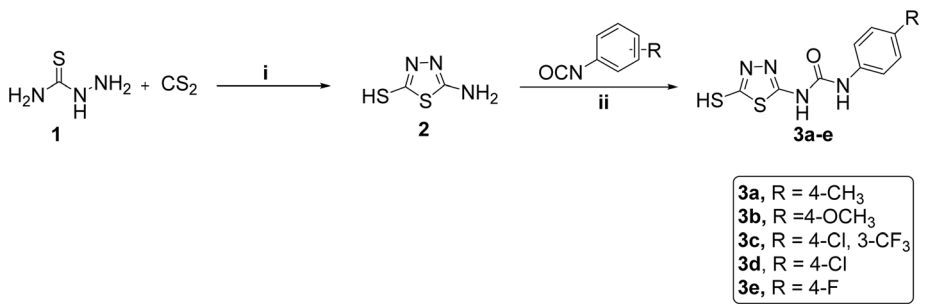

Scheme 1 Synthesis of 1,3,4-thiadiazole-aryl urea intermediates; reagents and conditions: (i) EtOH, reflux, 12 h, (ii) CH_3CN, reflux 12 h.

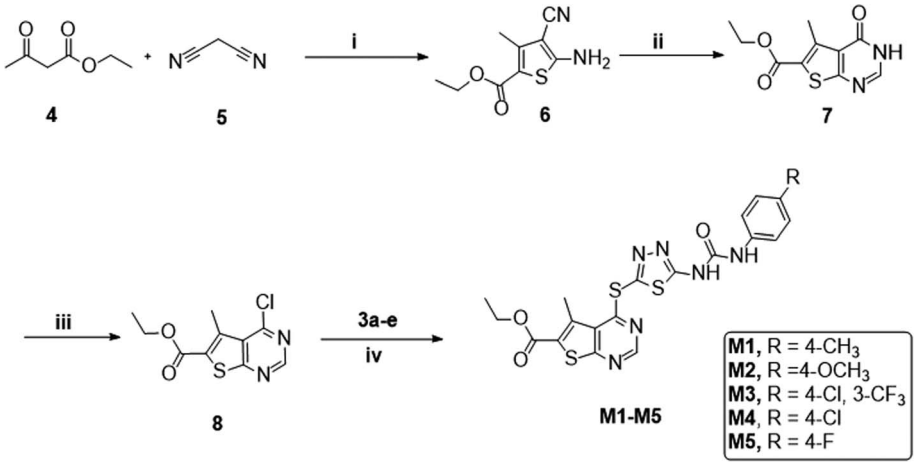

Scheme 2 Synthesis of the target thieno[2,3-*d*]pyrimidine derivatives (**M1–M5**); reagents and conditions: (i) S_8, Et_3N, EtOH, 90 °C, 12 h (ii) HCOOH, 120 °C, 12 h, (iii) $POCl_3$, 100 °C, 12 h, (iv) K_2CO_3, DMF, rt, 12 h.

2.3. Biological evaluation

2.3.1. *In vitro* anti-tumor activity. The cytotoxic evaluation of the target thieno[2,3-*d*]pyrimidine derivatives (**M1–M5**) across a panel of human tumor cell lines, including prostate adenocarcinoma (PC-3), cervical carcinoma (HeLa), liver carcinoma (HepG2), colorectal carcinoma (HCT-116), and two breast cancer cell lines (hormone receptor-positive MCF-7 and the triple-negative MDA-MB-231), demonstrated variable but notable antiproliferative activities. Among the tested compounds, **M1** (bearing a CH_3 substituent) exhibited the most potent and broad-spectrum activity, with IC_{50} values ranging from 3.61 μM (MCF-7) to 11.10 μM (PC-3). Remarkably, its activity against MCF-7 breast cancer cells (IC_{50} = 3.61 μM) was comparable to that of the reference drug Doxorubicin (IC_{50} = 4.17 μM) and substantially superior to Sorafenib (IC_{50} = 7.26 μM), positioning **M1** as a promising lead candidate for further development. In the MDA-MB-231 cells, **M1** also maintained relevant potency (IC_{50} = 5.37 μM), displaying a 3.6-fold improvement over Sorafenib (IC_{50} = 19.63 μM).

On the other hand, **M2** (OCH_3) and **M3** (4-Cl-3-CF_3) displayed relatively weak cytotoxic profiles, with IC_{50} values generally ≥30 μM across most cell lines. A moderate improvement was observed with the chloro-substituted derivative **M4**, particularly in HepG-2 cells (IC_{50} = 10.23 μM) and MCF-7 cells (IC_{50} = 6.93

Table 1 *In vitro* assessment of the cytotoxic effects of the tested compounds against a variety of cancer cell lines[b]

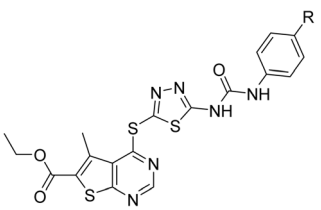

		IC_{50}[a] (μM ± SEM)					
Comp.	R	PC-3	Hela	HepG-2	HCT-116	MCF-7	MDA-MB-231
M1	4-CH_3	11.10 ± 0.8^{NS}	7.03 ± 0.5^{NS}	5.17 ± 0.4^{NS}	8.80 ± 0.5^{NS}	3.61 ± 0.2^{NS}	5.37 ± 0.42^{NS}
M2	4-OCH_3	$68.84 \pm 3.6^{*,\#}$	$47.46 \pm 2.8^{*,\#}$	$64.34 \pm 3.5^{*,\#}$	$52.65 \pm 3.1^{*,\#}$	$40.79 \pm 2.5^{*,\#}$	$29.33 \pm 5.25^{*}$
M3	4-Cl-3-CF_3	$54.06 \pm 3.2^{*,\#}$	$35.35 \pm 2.2^{*,\#}$	$49.72 \pm 2.8^{*,\#}$	$43.87 \pm 2.6^{*,\#}$	$29.52 \pm 1.9^{*,\#}$	$34.44 \pm 4.12^{*}$
M4	4-Cl	$21.52 \pm 1.5^{*}$	$16.14 \pm 1.3^{*,\#}$	$10.23 \pm 0.9^{*}$	12.07 ± 0.9^{NS}	6.93 ± 0.7^{NS}	$33.60 \pm 6.71^{*}$
M5	4-F	$38.17 \pm 2.4^{*,\#}$	$22.81 \pm 1.6^{*,\#}$	$33.59 \pm 2.2^{*,\#}$	$25.96 \pm 1.7^{*,\#}$	$14.64 \pm 1.2^{*,\#}$	$26.92 \pm 1.72^{*}$
DOX	—	8.87 ± 0.6	5.57 ± 0.4	4.50 ± 0.2	5.23 ± 0.3	4.17 ± 0.2	2.19 ± 0.22
SOR	—	11.53 ± 0.9	8.04 ± 0.5	9.18 ± 0.6	5.47 ± 0.3	7.26 ± 0.3	19.63 ± 2.87

[a] Data are presented as means of the IC_{50} values ± SEM based on three independent experiments. [b] $^{*}p < 0.05$ from Doxorubicin; $^{\#}p < 0.05$ from Sorafenib; "NS" represents non-significant from neither Doxorubicin nor Sorafenib "$p > 0.05$" using one-way analysis of variance (ANOVA) with the Tukey–Kramer test as a *post hoc* test. Stock solutions for each compound were prepared in DMSO. Eight concentrations (300, 100, 30, 10, 3, 1, 0.3, and 0.1 μM) were prepared for each compound in the growth media.

μM), although its effect against TNBC cells was limited (IC_{50} = 33.6 μM). Similarly, the fluoro-substituted analog **M5** demonstrated intermediate potency, with IC_{50} values in the range of 14–39 μM, showing moderate inhibition in MCF-7 (IC_{50} = 14.64 μM) but weaker activity against MDA-MB-231 (IC_{50} = 26.92 μM) (Table 1).

Taken together, these results indicate that the methyl-substituted scaffold **M1** confers superior cytotoxicity across most tested cancer models, especially breast cancer lines, with activity close to or surpassing that of standard therapeutics in select cases. Conversely, the incorporation of bulkier or strongly electron-withdrawing substituents in analogues **M2–M5** generally led to reduced activity, underscoring the sensitivity of the thienopyrimidine scaffold to both steric and electronic modifications. The enhanced potency of **M1** may be attributed to the small size and hydrophobic nature of the methyl group, which provides favorable hydrophobic interactions while maintaining minimal steric hindrance, allowing optimal accommodation within the binding sites of both VEGFR-2 and B-Raf sites without introducing steric hindrance. In contrast, bulkier substituents in **M2–M4** are likely to introduce steric clashes that impair proper ligand orientation and reduce binding affinity. Additionally, strongly electron-withdrawing substituents, as present in **M3–M5**, may unfavorably perturb the electronic distribution of the scaffold, weakening key hydrogen-bonding and π–π interactions essential for kinase inhibition.

2.3.2. *In vitro* cytotoxicity against human normal cells. The cytotoxicity evaluation against normal cell lines, including lung fibroblast (WI-38) and breast cells (MCF-10A), provided important insights into the safety and selectivity profile of the synthesized derivatives (Table 2). Compound **M1**, while demonstrating the strongest anticancer activity among the series, displayed low cytotoxicity toward normal cells with IC_{50} values of 31.22 μM (WI-38) and 27.51 μM (MCF-10A). These values correspond to a favorable therapeutic window compared with its sub-micromolar potency in cancer cells, suggesting a cancer-selective mechanism of action. In contrast, the clinically approved multi-kinase inhibitor Sorafenib exhibited higher toxicity in normal fibroblasts (IC_{50} = 10.65 μM in WI-38), whereas the standard chemotherapeutic Doxorubicin was considerably more toxic to both WI-38 (IC_{50} = 6.72 μM) and MCF-10A (IC_{50} = 12.20 μM), reflecting its well-known safety limitations. Other synthesized derivatives, particularly **M2–M5**, showed reduced cytotoxicity in normal cells (IC_{50} values of up to 76.32 μM in WI-38 and 81.18 μM in MCF-10A). Together, these findings underscore **M1** as a promising candidate that combines potent anticancer activity with an acceptable safety profile.

2.3.3. *In vitro* aurora B and VEGFR-2 kinases inhibition assay. The inhibitory activity of compounds **M1–M5** on Aurora B and VEGFR-2 kinases was evaluated for dose-dependent enzymatic inhibition at 8 distinct concentrations to determine their IC_{50} values, using Aurora B and VEGFR-2 inhibition assay kits. The results in Table 3 clearly indicate that compound **M1** is the most potent dual inhibitor of VEGFR-2 and Aurora B among the synthesized derivatives, with IC_{50} values of 0.220 ± 0.02 μM and 0.037 ± 0.01 μM, respectively. Compared with the reference VEGFR-2 inhibitor Sorafenib (IC_{50} = 0.055 μM), **M1** displayed nearly fourfold lower VEGFR-2 inhibitory potency; however, **M1** surpassed Sorafenib by additionally exhibiting strong Aurora B inhibition, placing it closer to the reference Aurora B inhibitor SP-96 (IC_{50} = 0.020 μM). In contrast, **M2–M4** showed considerably weaker dual inhibition, with micromolar-range IC_{50} values, indicating a loss of balanced activity against both targets. Interestingly, although **M5** exhibited the strongest VEGFR-2 inhibition among the series (IC_{50} = 0.141 μM, approaching Sorafenib's potency), its weaker Aurora B inhibition (IC_{50} = 0.705 μM) highlights the lack of equipotency required for an effective dual-target profile. Overall, the marked enzymatic potency of **M1** against Aurora B, combined with its sub-micromolar VEGFR-2 inhibition, supports its identification as the most promising dual kinase inhibitor in this series at the biochemical level. Further cellular target-engagement studies are required to confirm direct inhibition within biological systems.

2.3.4. Assessment of cell cycle distribution in TNBC cells MDA-MB-231 after M1 treatment. Treatment of MDA-MB-231

Table 2 *In vitro* cytotoxicity of the tested compounds M1–M5 against two normal human cell lines: lung-derived fibroblasts (WI-38) and normal breast epithelial cells (MCF-10A) after 48 hours of treatment[b]

	IC_{50}[a] (μM ± SEM)	
Comp.	WI-38	MCF-10A
M1	31.22 ± 2.1$^{*,\#}$	27.51 ± 6.20^{NS}
M2	27.19 ± 1.8$^{*,\#}$	81.18 ± 11.62$^{*,\#}$
M3	62.93 ± 3.5$^{*,\#}$	55.61 ± 7.59*
M4	58.66 ± 3.3$^{*,\#}$	58.41 ± 6.57*
M5	76.32 ± 3.8$^{*,\#}$	42.82 ± 7.08 ^{NS}
Sorafenib	10.65 ± 0.8	47.06 ± 4.99
Doxorubicin	6.72 ± 0.5	12.20 ± 2.64

[a] Data are presented as means of the IC_{50} values ± SEM based on three independent experiments. [b] $^{*}p < 0.05$ from Doxorubicin; $^{\#}p < 0.05$ from Sorafenib; "NS" represents non-significant from either Doxorubicin or Sorafenib "$p > 0.05$" using one-way analysis of variance (ANOVA) with the Tukey–Kramer test as a *post hoc* test.

Table 3 IC_{50} values of the target compounds as Aurora kinase B and VEGFR-2 inhibitors[b]

	IC_{50}[a] (μM ± SEM)	
Comp.	Aurora B	VEGFR-2
M1	0.037 ± 0.01^{NS}	0.220 ± 0.02^{NS}
M2	0.529 ± 0.11^{NS}	1.122 ± 0.39$^{\#}$
M3	3.469 ± 0.17*	1.298 ± 0.16$^{\#}$
M4	1.673 ± 0.55*	2.979 ± 0.17$^{\#}$
M5	0.705 ± 0.09^{NS}	0.141 ± 0.04^{NS}
SP-96	0.020 ± 0.002	—
Sorafenib	—	0.055 ± 0.01

[a] Data are presented as means of the IC_{50} values ± SEM based on three independent experiments. [b] $^{*}p < 0.05$ indicates statistical significance from SP-96; $^{\#}p < 0.05$ indicates statistical significance from Sorafenib; "NS" represents non-significant from the corresponding standard. The significance of data was analyzed using one-way analysis of variance (ANOVA) with the Tukey–Kramer test as a *post hoc* test.

Table 4 Impact of compound **M1** on cell cycle progression in MDA-MB-231 cells following 48 h of treatment

	Cell cycle distribution[a] (%)			
Sample	%Sub-G1	%G1	%S	% G2/M
MDA-MB-231	5.96 ± 0.22	56.42 ± 2.13	8.25 ± 0.44	29.37 ± 1.71
M1/MDA-MB-231	2.34 ± 0.26[b]	72.47 ± 2.02[b]	17.11 ± 0.95[b]	8.08 ± 0.45[b]

[a] Percentage distribution of MDA-MB-231 cells across the cell cycle phases with and without treatment by compound **M1**. Values are given as mean ± SEM ($n = 3$). [b] $p < 0.05$ indicates statistically significant differences from the corresponding control (MDA-MB-231) group in unpaired *t*-tests.

cells with compound **M1** led to a pronounced cell cycle modulation compared with untreated controls, consistent with its dual Aurora B and VEGFR-2 inhibitory activity (Table 4 and Fig. 5). In the control, the majority of cells were distributed in the G1 (56.42%) and G2/M (29.37%) phases, reflecting the characteristic proliferative profile of this aggressive triple-negative breast cancer line. Upon **M1** treatment, there was a significant G1 phase accumulation (72.47%) accompanied by a marked reduction in the G2/M population (8.08%), suggesting that **M1** effectively halts cell cycle progression by inducing a strong G1 arrest. This shift was paralleled by an increase in the S-phase population (17.11% *vs.* 8.25% in controls), further indicating cell cycle dysregulation and proper inhibition of cell cycle transition.

2.3.5. Apoptotic effect of compound M1 on TNBC cells MDA-MB-231. To determine whether compound **M1** mediates its anticancer effects through apoptotic mechanisms, we evaluated its impact on apoptotic cell populations in MDA-MB-231 cells. As presented in Table 5 and Fig. 6, apoptosis analysis revealed a striking decrease in viable cell population (from 97.51% in untreated cells to 54.55% with **M1**) with concomitant increases in both early (24.13%) and late apoptosis (19.99% *vs.* <1% in controls). Necrosis remained minimal (1.33%), suggesting that **M1** preferentially induces programmed rather than non-specific cell death. Taken together, these findings indicate that **M1** exerts its anticancer effect in MDA-MB-231 cells primarily through induction of G1 cell cycle arrest and

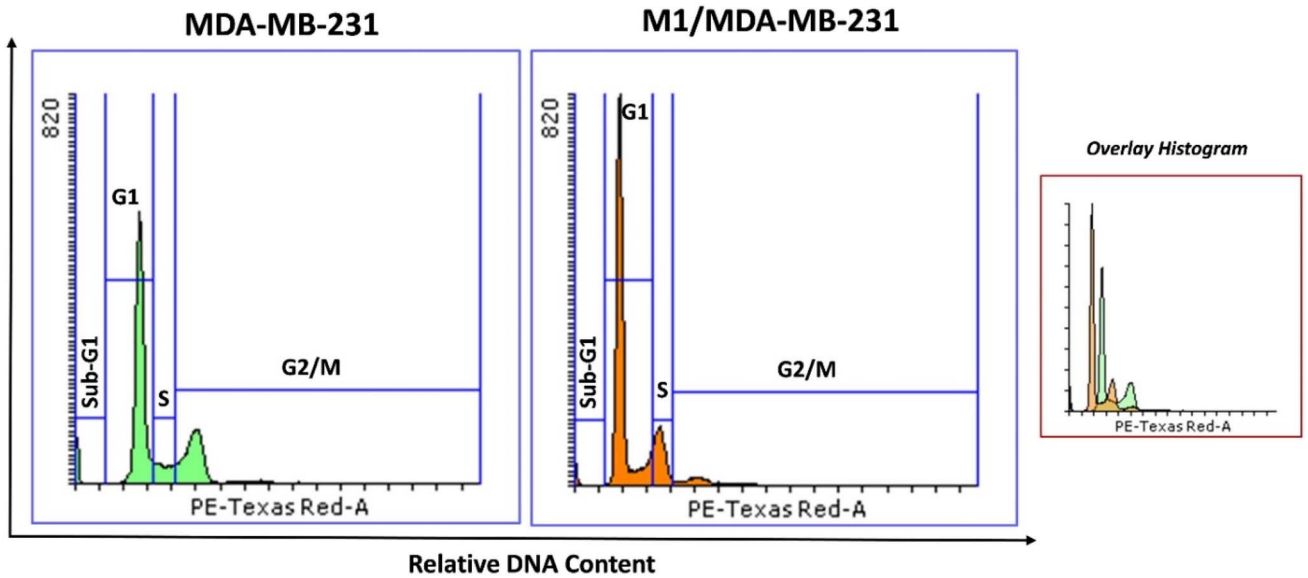

Fig. 5 Flow cytometric assessment of cell cycle phase distribution following treatment with the compound **M1**.

Table 5 Impact of compound **M1** on the different stages of cell death in MDA-MB-231 cells following 48 hours of treatment[b]

		Apoptosis[a]		
Sample	Viable[a] (left bottom)	Early (right bottom)	Late (right top)	Necrosis[a] (left top)
MDA-MB-231	97.51 ± 0.80%	0.48 ± 0.12%	1.30 ± 0.12%	0.71 ± 0.09%
M1/MDA-MB-231	54.55 ± 0.84%*	24.13 ± 0.92%*	19.99 ± 0.83%*	1.33 ± 0.12%NS

[a] Values are given as mean ± SEM ($n = 3$). [b] *$p < 0.05$ indicates statistically significant differences from the corresponding control (MDA-MB-231) group in unpaired *t*-tests; "NS" represents non-significant from the corresponding control (MDA-MB-231) group.

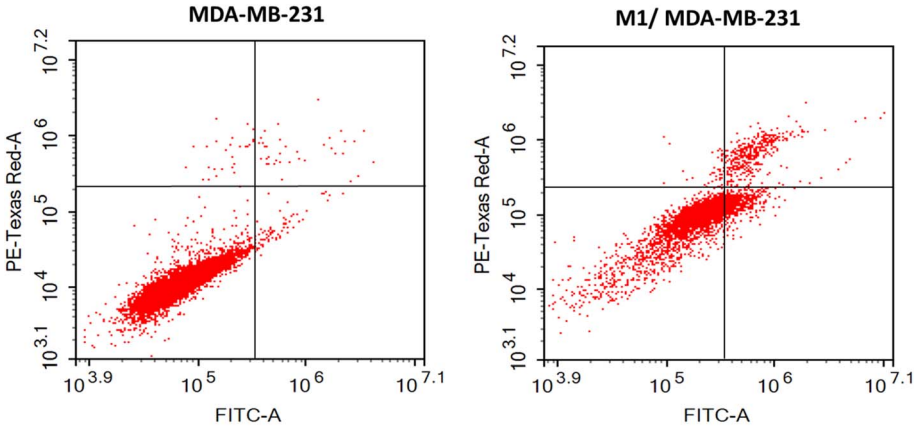

Fig. 6 Flow cytometric evaluation of apoptosis in MDA-MB-231 cells treated with compound **M1** at its IC_{50} concentration (5.37 μM) for 48 hours.

activation of apoptotic pathways, highlighting its potential as a therapeutic candidate against TNBC.

2.3.6. Assessment of pro- and anti-apoptotic marker expression following M1 treatment. To further elucidate the molecular mechanism underlying **M1**-induced apoptosis, the expression of key apoptosis-regulating proteins was assessed by western blotting in MDA-MB-231 cells. Treatment with **M1** resulted in a pronounced upregulation of the pro-apoptotic protein Bax and a concomitant downregulation of the anti-apoptotic protein Bcl-2 relative to untreated control cells. Densitometric analysis revealed that Bax expression increased by approximately 3.1-fold, whereas Bcl-2 expression was reduced to 0.54-fold of control levels, with β-actin used as a loading control. Consequently, the Bax/Bcl-2 ratio was markedly elevated by about 5.8-fold, indicating activation of the intrinsic mitochondrial apoptotic pathway (Table 6 and Fig. 7). These molecular findings are fully consistent with the apoptosis induction observed by flow cytometric analysis and further support the pro-apoptotic effect of **M1** at the protein level.

2.3.7. Cellular validation of VEGFR-2 downstream signaling inhibition. To further confirm downstream target engagement beyond enzymatic inhibition, the effect of the most active compound **M1** on VEGFR-2-related signaling pathways was evaluated in MDA-MB-231 cells. Treatment with **M1** resulted in a marked suppression of VEGFR-2 downstream effectors, as evidenced by significant reductions in phosphorylated STAT3 (p-STAT3) and phosphorylated ERK1/2 (p-ERK1/2) levels. p-STAT3 levels decreased from 61.46 ± 2.11 ng mL^{-1} in control cells to 36.22 ± 1.24 ng mL^{-1}, corresponding to approximately a 1.7-fold reduction. Likewise, **M1** significantly suppressed p-ERK1/2, with its concentration decreasing from 366.26 ± 14.20 pg mL^{-1} in control cells to 156.02 ± 6.06 pg mL^{-1}, representing about a 2.3-fold reduction (Table 7). Collectively, since STAT3 and ERK1/2 function as downstream effectors of VEGFR-2 signaling, these findings suggest that the inhibition of VEGFR-2 signaling is inferred from biochemical assays and downstream pathway modulation rather than direct cellular phosphorylation analysis.

2.3.8. *In vivo* evaluation of compound M1's anti-breast cancer activity and its impact on Caspase-3 apoptotic marker levels. The *in vivo* potency of compound **M1** was further evaluated employing a DMBA-induced breast cancer model, with tumor volume progression and body weight changes monitored over 20 days (Fig. 8 and Table 8). In the untreated DMBA group, continuous tumor growth was observed, with a mean tumor volume reaching 2.07 ± 0.08 mm^3 by day 20, accompanied by a marked increase in body weight (42.2 ± 0.96 g), reflecting both

Table 6 Effect of **M1** on pro-apoptotic (Bax) and anti-apoptotic (Bcl-2) protein expression in MDA-MB-231 cells

	OD values	
Compound	Bax	Bcl2
MDA-MB-231	1.921	3.963
M1/MDA-MB-231	5.951	2.123

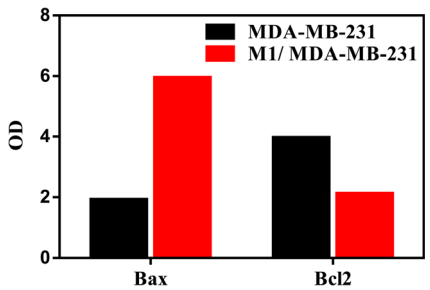

Fig. 7 Densitometric analysis (OD values) of Bax and Bcl-2 protein expression in MDA-MB-231 cells following **M1** treatment, as determined by western blot analysis.

Table 7 Effect of **M1** treatment on p-STAT3 and p-ERK1/2 expression levels in MDA-MB-231 cells[a]

Compound	p-STAT3 (ng mL^{-1})	p-ERK1/2 (pg mL^{-1})
MDA-MB-231	61.461 ± 2.11	366.26 ± 14.2
M1/MDA-MB-231	36.217 ± 1.24	156.02 ± 6.06

[a] Values were reported as mean ± SD of three independent experiments.

tumor burden and systemic metabolic dysregulation. In contrast, treatment with the reference drug Doxorubicin significantly inhibited tumor progression, resulting in only 0.73 ± 0.05 mm^3 by day 20 (64.8% reduction *vs.* DMBA), but was associated with notable body weight loss (21.8% reduction), consistent with its known systemic toxicity. Interestingly, **M1** demonstrated a comparable antitumor effect, suppressing tumor growth to 0.86 ± 0.05 mm^3 (58.6% reduction *vs.* DMBA), and its efficacy was statistically indistinguishable from that of Doxorubicin across the studied time points. Importantly, unlike Doxorubicin, **M1** treatment was associated with a more favorable systemic tolerability profile, as reflected by a lower reduction in body weight (13.7%), suggesting that **M1** exerted effective tumor suppression with reduced systemic toxicity. Collectively, these findings highlight the therapeutic promise of **M1**, which demonstrates substantial antitumor potency *in vivo* with an improved safety margin compared to the clinically used agent Doxorubicin.

Histopathological and immunohistochemical analyses further confirmed the anticancer potential of compound **M1**. As shown in Fig. 9, examination of hematoxylin and eosin (H&E)-stained mammary gland sections from the DMBA-induced group revealed marked pathological alterations, including atypical ductal hyperplasia, nuclear pleomorphism, extensive fibrosis, and pronounced inflammatory cell infiltration, all consistent with malignant transformation. In contrast, Doxorubicin treatment attenuated these changes, resulting in only mild ductal hyperplasia with limited fibrotic and inflammatory responses. Similarly, tissues from the **M1**-treated group demonstrated a notable improvement compared to the DMBA group, characterized by mild acinar hyperplasia with moderate fibrous tissue deposition and reduced inflammatory infiltration, suggesting significant regression of malignant progression.

These findings were further supported by complementary immunohistochemical staining for caspase-3, a critical mediator of apoptosis (Fig. 10 and 11). The DMBA-induced group displayed almost complete loss of caspase-3 expression (IHC score 0.16), reflecting impaired apoptotic activity in tumor tissue. Doxorubicin markedly enhanced caspase-3 activation (IHC score 1.83), consistent with its well-documented pro-apoptotic effect. Importantly, the **M1**-treated group also showed a significant upregulation of caspase-3 expression (IHC score 1.33) compared to the DMBA group, albeit slightly lower than Doxorubicin, indicating restoration of apoptotic signalling as a key mechanism underlying its anticancer effect. Together, these histopathological and molecular findings confirm that **M1** not only suppresses tumor growth *in vivo* but also ameliorates tumor-associated structural abnormalities and promotes apoptotic cell death within breast tissues. A notable limitation of these studies is that direct cellular engagement of Aurora B and VEGFR-2 was not assessed. The dual kinase inhibitory activity of **M1** is supported by biochemical assays and consistent downstream cellular phenotypes; however, direct phosphorylation assays or target-engagement studies (*e.g.*, histone H3 Ser10 immunoblotting) are needed to fully confirm intracellular on-target activity.

2.4. Computational investigation

2.4.1. Molecular docking. To explore the potential binding pattern of the selected and reference compounds within the

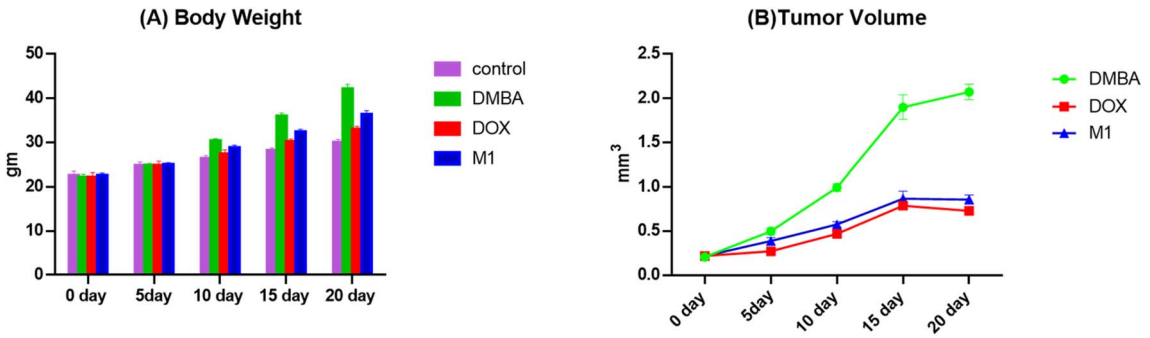

Fig. 8 Graphical illustration of the changes in body weight (A) and tumor volume (B) over 20 days in mice with DMBA-induced tumors. The groups involve untreated control, DMBA-only, and DOX-treated and **M1**-treated mice.

Table 8 Effect of compound **M1** on tumor volume and body weight in DMBA-induced breast cancer mice following 20 days of treatment[a]

Compound	Mean tumor volume (mm^3)	% Tumor volume reduction	Mean body weight (g)	% Body weight reduction
DMBA	2.074 ± 0.080	—	42.2 ± 0.96	—
DOX	0.73 ± 0.047	64.80	33 ± 0.70	21.80
M1	0.858 ± 0.050	58.63	36.4 ± 0.81	13.74

[a] The percentage reduction in tumor volume and body weight was calculated *via* subtracting mean tumor volume/body weight (vol/wt) of the treated group from the vol/wt of the DMBA group, divided by vol/wt of the DMBA group, times 100. DMBA represents the pre-therapy group, and the treated groups include DOX and compound **M1**.

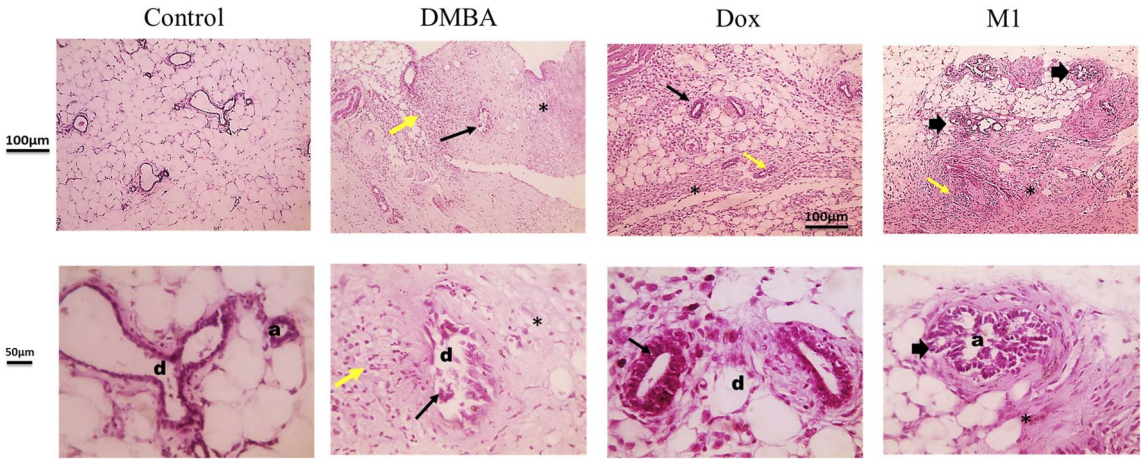

Fig. 9 Histopathological examination of mammary gland tissues (H&E stain). Representative micrographs of non-lactating mammary gland sections from control group, DMBA-induced group, DOX-treated group, and **M1**-treated group. The control normal group shows normal duct (d) and acini (a) embedded in adipose tissue with no pathological lesions. DMBA group exhibits atypical hyperplasia characterized by disorganized cell layers with nuclear pleomorphism (d) (thin black arrow), dead cells present in their lumens surrounded by severe fibrous tissue deposition (*) and many inflammatory cells infiltration (yellow arrow). DOX-treated tissues show mild ductal hyperplasia characterized by bilayer of columnar ductal cells (d) (thin black arrow) surrounded by mild fibrous tissue deposition (*) with few inflammatory cells' infiltration (yellow arrow). **M1** treated group shows of mild acinar hyperplasia (a) (thick black arrow), accompanied by moderate fibrous tissue deposition (*) with some inflammatory cells' infiltration (yellow arrow). Images are displayed at low magnification (100×; scale bar = 100 μm) and high magnification (400×; scale bar = 50 μm).

VEGFR-2 and Aurora B binding sites, we used a comprehensive *in silico* approach based on molecular docking and dynamics simulation. Fig. 12 and Table 9 display the molecular docking output of compound **M1** within the binding sites of VEGFR-2 (Fig. 12A) and Aurora B (Fig. 12B). Compound **M1** strongly interacts with both targets, showing several polar and hydrophobic contacts. Considering the VEGFR-2 binding site, compound **M1** is predicted to target N923 and L840 *via* a strong H-bond network. Furthermore, additional H-bonds were found with the R1051 and K1055 side chains. Non-polar interactions were found with F1047 (π–π stacking), L840, F918, G922, and L1035 (hydrophobic interactions). This binding configuration resulted in a docking score of −8.268 kcal mol^{-1} (Table 9), suggesting the strong binding affinity of compound **M1** for the target protein. Furthermore, compound **M1** also demonstrated a clear capacity to interact with Aurora B (Fig. 12B). A strong network of polar contacts with Y156, A157, and P158 residues was detected. In addition, compound **M1** can establish several non-polar contacts with residues K106 (cation–π stacking), L83, F88, L154, A157, P158, and F219 (hydrophobic interactions). The proposed binding configuration yielded a docking score of −8.783 kcal mol^{-1} (Table 9), suggesting that the compound can strongly interact with the selected target.

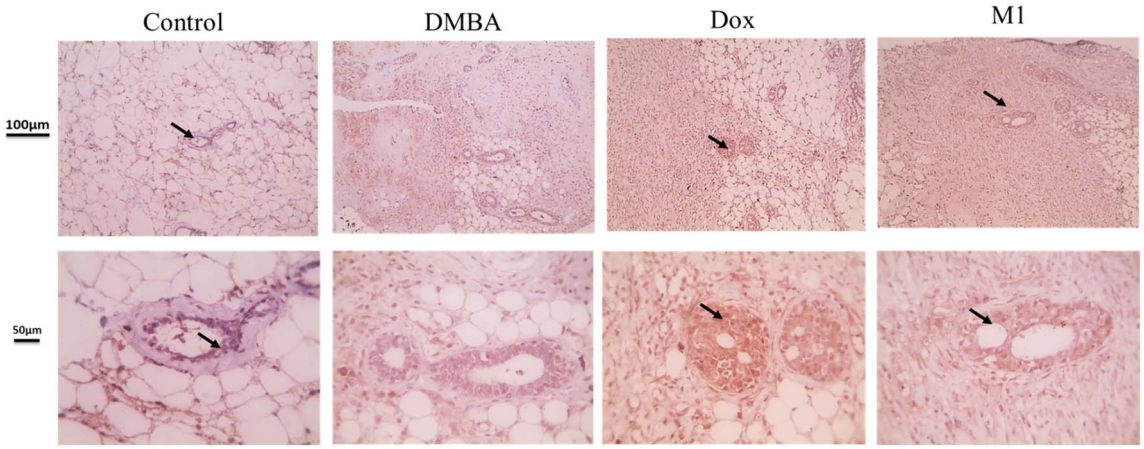

Fig. 10 Immunohistochemical staining for caspase-3 expression. Representative micrographs of non-lactating mammary gland sections from control group, DMBA-induced group, DOX-treated group, and **M1**-treated group. The control group shows mild positive brown expression against caspase-3 (black arrow). The DMBA group is mostly negative. The **M1**-treated group exhibits fewer positive cells (black arrows) compared to the DOX-treated group (black arrow). IHC was counterstained using Mayer's hematoxylin. Images shown at low magnification (100×; scale bar = 100 μm) and high magnification (400×; scale bar = 50 μm).

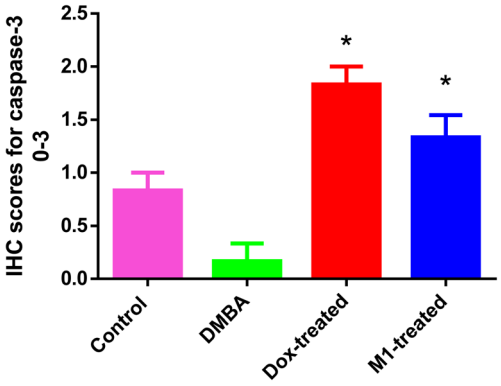

Fig. 11 Quantitative analysis of caspase-3 immuno-expression. Bar chart representing the mean immunohistochemical (IHC) scores (mean ± SE) of caspase-3 expression in mammary gland tissues for control, DMBA, Doxorubicin, and **M1** treatment groups. Caspase-3 expression was significantly suppressed in the DMBA group (IHC score = 0.16) compared to the control (0.83). Both Doxorubicin (1.83) and **M1** (1.33) significantly restored caspase-3 expression relative to the DMBA model ($P < 0.05$), consistent with their ability to promote apoptosis. Statistical analyses were conducted using the Kruskal–Wallis test followed by Dunn's *post hoc* test.

Considering compound **M5** within the VEGFR-2 and Aurora B binding sites, we found comparable binding modes with respect to the docking results found for compound **M1**. This was largely expected due to the small change in the chemical structure of compounds **M1** and **M5**. In fact, considering VEGFR-2 (Fig. 13A and Table 9), compound **M5** can establish the same polar and non-polar interactions previously discussed for compound **M1** with the key residues of the binding site (N923, L840, R1051, and K1055, H-bonds; F1047, π–π stacking; L840, F918, G922, and L1035, hydrophobic interactions). This binding pose yielded a docking score of −7.981 kcal mol^{-1} (Table 9), suggesting that the small change in the chemical structure of **M5** was compatible with the binding site of the target kinase. The same trend was observed when compound **M5** was docked into the binding pocket of Aurora B (Fig. 13B). In fact, compound **M5** was able to target the same residues previously discussed for compound **M1** (Y156 and A157, H bonds; K106, cation–π stacking; L83, F88, L154, A157, P158, and F219, hydrophobic interactions), with the exclusion of the polar contacts with P158. The retrieved binding pose produced a docking score of −8.630 kcal mol^{-1} (Table 9), suggesting, also in this case, a strong capability of the compound to interact with the selected target. In addition, we evaluated the docking scores of reference compounds Sorafenib and VX-680 within the VEGFR-2 and Aurora B binding sites, respectively. These reference compounds were the native ligand of the crystal structure used for molecular docking calculation and can provide a direct comparison among the retrieved binding modes. In particular, we found a more favorable docking score for Sorafenib, although the targeted residues and VEGFR-2 binding site occupancy were similar to those observed for the developed compounds **M1** and **M5** (Table 9). Sorafenib targeted F918, C919, E885, and D1046 *via* H-bonds, whereas a π–π stacking was established with F1047. Strong hydrophobic interactions were detected with L840, F918, G922, and L1035. Accordingly, the slight improvement in the number of contacts within the selected binding site along with favorable docking scores with respect to the developed compounds **M1** and **M5** may contribute to a moderate improvement in the inhibitory capacity against VEGFR-2 as indicated by the assay on the isolated protein. Regarding Aurora B, the reference compound VX-680 showed a similar binding mode, as observed in the crystal structure, with respect to **M1** and **M5**. In fact, VX-680 established a strong H-bond network with K106, E155, and A157 H-bonds and a π–π stacking with F88. Hydrophobic interactions were detected with residues L83, L154, Y156, A157, P158, and F219. The docking score of VX-680 is comparable to those of **M1** and **M5** (Table 9), and it is consistent with the inhibitory capacity of compounds against Aurora B.

Table 9 Docking scores (kcal mol^{-1}) of the developed and reference ligands

	Docking score (kcal mol^{-1})	
Compound	VEGFR-2	Aurora B
M1	−8.268	−8.783
M5	−7.981	−8.630
Sorafenib	−10.763	—
VX-680	—	−9.354

2.4.2. Molecular dynamics. To improve the quality of the calculation, we performed molecular dynamics simulation

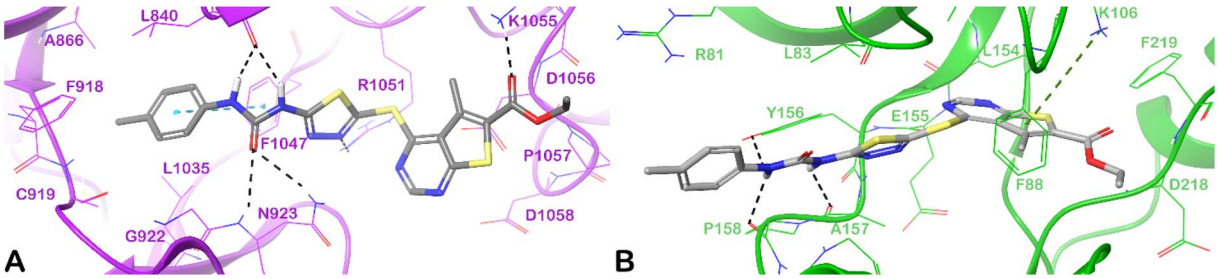

Fig. 12 Putative binding modes of compound **M1** (gray sticks) within the binding sites of VEGFR-2 (purple cartoon, PDB ID 4ASD, panel (A)) and Aurora B (green cartoon, PDB ID 4AF3, panel (B)). Binding site residues are depicted as lines, with hydrogen bonds represented by black dotted lines, and π–π and cation–π stacking interactions indicated by cyan and dark green dotted lines, respectively. The images were created using Maestro software (Schrödinger, LLC, New York, 2020).

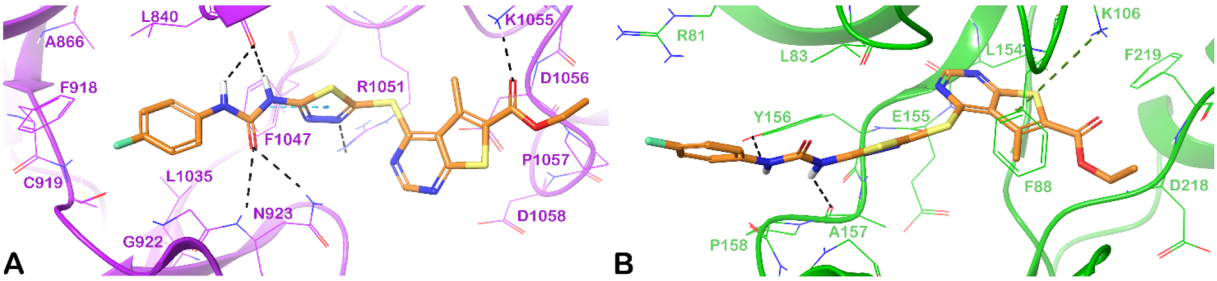

Fig. 13 Putative binding modes of compound **M5** (orange sticks) within the VEGFR-2 (purple cartoon, PDB ID 4ASD, panel (A)) and Aurora B (green cartoon, PDB ID 4AF3, panel (B)) binding sites. Binding site residues are depicted as lines, with hydrogen bonds represented by black dotted lines, and π−π and cation−π stacking interactions indicated by cyan and dark green dotted lines, respectively. The images were created using Maestro software (Schrödinger, LLC, New York, 2020).

studies on the ligands **M1** and **M5** and reference drugs Sorafenib and VX-680 within the VEGFR-2 and Aurora B binding sites, starting from the complexes gained from docking calculations. Fig. 13, 14 and Table 10 show the output of the simulations, indicating a general stability of the binding of the tested compounds within both binding sites as indicated by the RMSD calculation. In particular, considering VEGFR-2 (Fig. 14), **M1** was able to maintain the contacts acquired by molecular

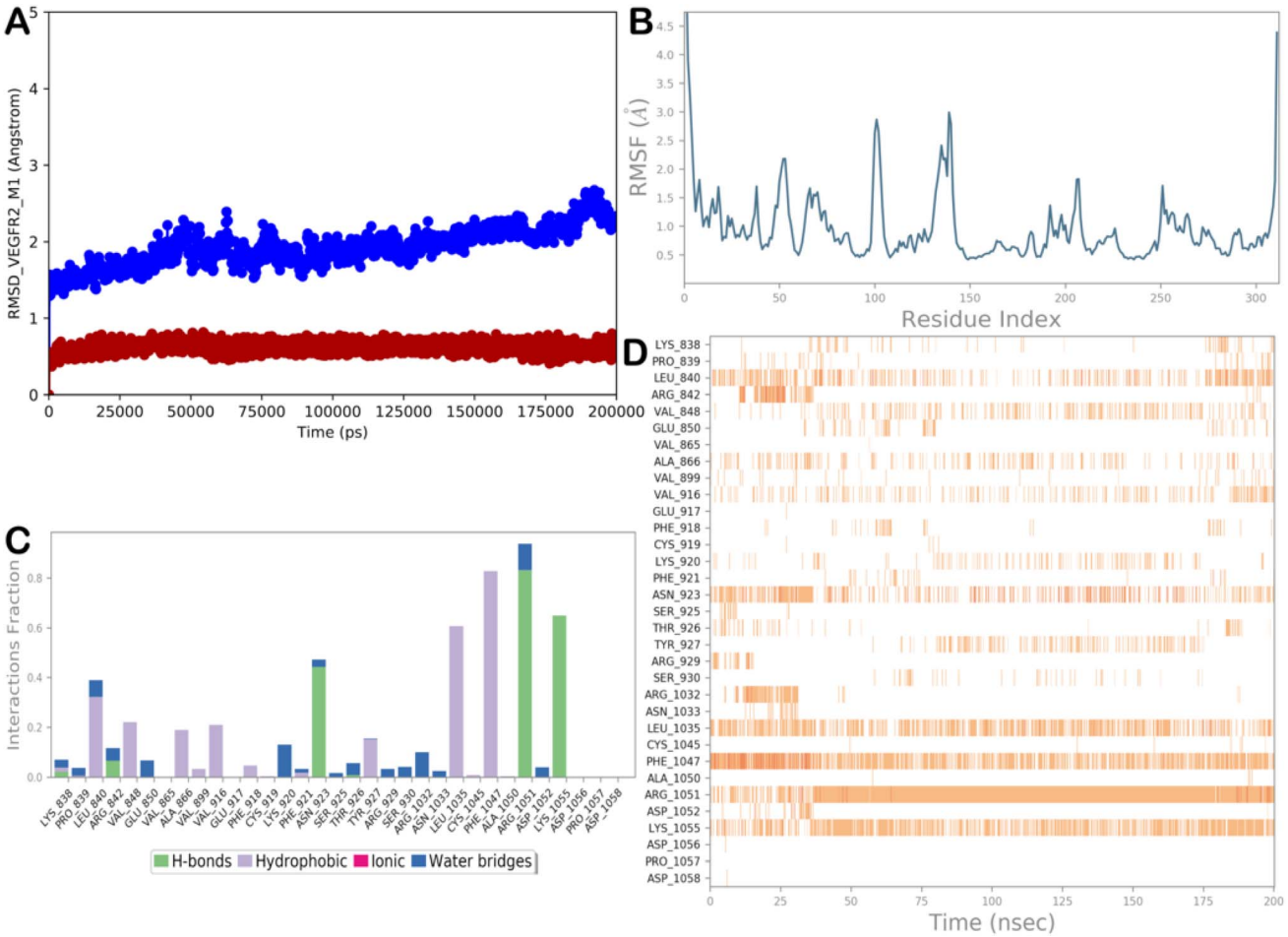

Fig. 14 (A) RMSD analysis (protein: blue line; and ligand: red line). (B) RMSF evaluation for the VEGFR-2/**M1**, derived from docking studies, after a 200 ns molecular dynamics simulation. (C and D) Visualization of compound **M1** during the molecular dynamics trajectory, highlighting four types of interactions: water bridges (blue), ionic contacts (magenta), hydrophobic interactions (grey), and hydrogen bonds (green). The stacked bar charts represent normalized contact frequencies, where a value of 0.7 means the interaction was maintained 70% of the simulation time. Values exceeding 1.0 indicate multiple contacts between a protein residue and the ligand. The timeline diagram illustrates key interactions over the simulation. Residues interacting with the ligand at each frame are indicated, with darker orange showing residues forming multiple contacts. Images were generated using Maestro and Desmond software (Maestro, Schrödinger LLC, release 2020-3).

Table 10 Predicted binding free energies (ΔG_{bind}) and the main energy components of the selected compounds, as determined by MM/GBSA calculations

Compound ID	ΔG_{vdw}[a] (kcal mol^{-1})	ΔG_{coul}[b] (kcal mol^{-1})	ΔG_{Hbond}[c] (kcal mol^{-1})	ΔG_{Lipo}[d] (kcal mol^{-1})	ΔG_{Pack}[e] (kcal mol^{-1})	ΔG_{SolGB}[f] (kcal mol^{-1})	ΔG_{bind}[g] (kcal mol^{-1})
VEGFR-2							
M1	−53.74	−9.87	−2.37	−21.38	−1.89	17.02	−72.43
M5	−56.13	−10.26	−1.97	−22.29	−2.47	18.34	74.75
Sorafenib	−60.88	−11.95	−2.29	−25.76	−1.24	20.79	−81.29
Aurora B							
M1	−61.48	−13.52	−2.26	−20.41	−2.10	16.18	−83.74
M5	−57.39	−11.86	−1.32	−17.73	−2.44	15.52	−75.61
VX-680	−63.22	−15.89	−2.08	−21.87	−2.19	19.81	−85.16

[a] Contribution of van der Waals interaction energy to binding free energy. [b] Contribution of Coulomb energy to binding free energy. [c] Hydrogen-bonding contributions to binding free energy. [d] Lipophilic energy contribution to binding free energy. [e] π–π packing energy contribution to binding free energy. [f] Generalized Born electrostatic solvation energy contribution to binding free energy. [g] Total binding free energy.

docking, being able to constantly target residues N923, R1051, and K1055 *via* polar interactions. Hydrophobic contacts continue to be important for the binding of **M1** since it established π–π stacking with F1047 for all the simulation. Moreover, strong hydrophobic interactions were observed with residues L840 and L1035. Additional contacts with V848, A866, V916, F918, and T927 were detected, which contributed to the stabilization of the identified binding mode.

The molecular dynamics simulation of the Aurora B/**M1** complex (Fig. 15) revealed the general stability of the system, including the binding mode of the compound, as shown by the RMSD and RMSF calculations. The binding mode of the compound presented small changes with respect to the binding pose retrieved by molecular docking calculation. In fact, the polar and hydrophobic interaction with residues L83, F88, Y156, A157, and P158 were strongly maintained during the simulation, whereas the interactions with K106, L154, and F219 became sporadic. Interestingly, additional hydrophobic contacts with residues R81 (mainly cation–π stacking) and L138 were observed and contributed to the stability of the binding pose of **M1** within the Aurora B binding pocket.

Fig. 16 and 17 show the output of the simulations of compound **M5** within the selected binding sites, indicating a general stability of the binding of compound **M5** within both binding sites, as indicated by the RMSD and RMSF calculations. In particular, considering VEGFR-2 (Fig. 16), **M5** was able to maintain the key contacts identified by molecular docking calculation. The H-bonds with residues N923, L840, R1051, and K1055 were detected for all the simulation, as well as the π–π stacking with F1047. Hydrophobic interactions with L840 and L1035 were constantly observed, whereas the targeting of residues F918 and G922 became sporadic and was replaced by a more favorable hydrophobic interaction with A866.

Compound **M5** inside the Aurora B binding site exhibited general stability with persistent Y156 and A157 residue targeting *via* H bonds and limited system fluctuations (Fig. 17). The hydrophobic interactions with K106 (cation–π stacking) continued to be evident as well as the hydrophobic interactions with residues L83, F88, and L154. In addition, we noted the formation of interactions with R81, K85, and L138, whereas the contacts with F219 became sporadic.

To better circumstantiate the findings on the developed compounds, we compared them with the reference drugs. In particular, we calculated the ΔG_{bind} of **M1**, **M5**, Sorafenib, and VX-680 within the targeted proteins using the entire simulation trajectories to have a direct comparison of the affinity of compounds against the selected binding sites (Table 10). Regarding the VEGFR-2, from the calculation is evident the strong contribution of van der Waals interactions to the ΔG_{bind}, and in general the lipophilic content of the compounds. H-bonds and polar interactions contributed to the stabilization of the binding, and in this sense, Sorafenib showed a better energetic profile, with the most significant contribution to the ΔG_{bind} derived from van der Waals interactions, whereas the other energetic terms were largely comparable with those found for the compounds **M1** and **M5**. Accordingly, this significant contribution to the ΔG_{bind} is highlighted by the inhibitory capacity of Sorafenib, which was found to be one order of magnitude more potent than **M1** and **M5**. Considering Aurora B, the energetic profile of the reference compound VX-680 was largely comparable with that of compound **M1**. In fact, the contribution to ΔG_{bind} of van der Waals and H-bonds and polar interactions was similar for both compounds (VX-680 and **M1**), whereas **M5** showed less favorable energetic terms regarding the hydrophobic interactions and H-bonds (Table 10). These results indicate that while **M1** shows promising computational binding characteristics, the reference ligands generally display more favorable binding energies. Notably, the ΔG_bind calculations using the MM/GBSA method were more consistent with experimental binding affinities than docking scores alone, providing a more reliable, yet still comparative, computational assessment.

2.5. Assessment of aqueous solubility and lipophilicity profile

The compound **M1** exhibited very low aqueous solubility in PBS (pH 7.4), with an equilibrium solubility of 1.11 ± 0.06 μg mL^{-1} after 2 h of sonication. Despite the low aqueous solubility, the

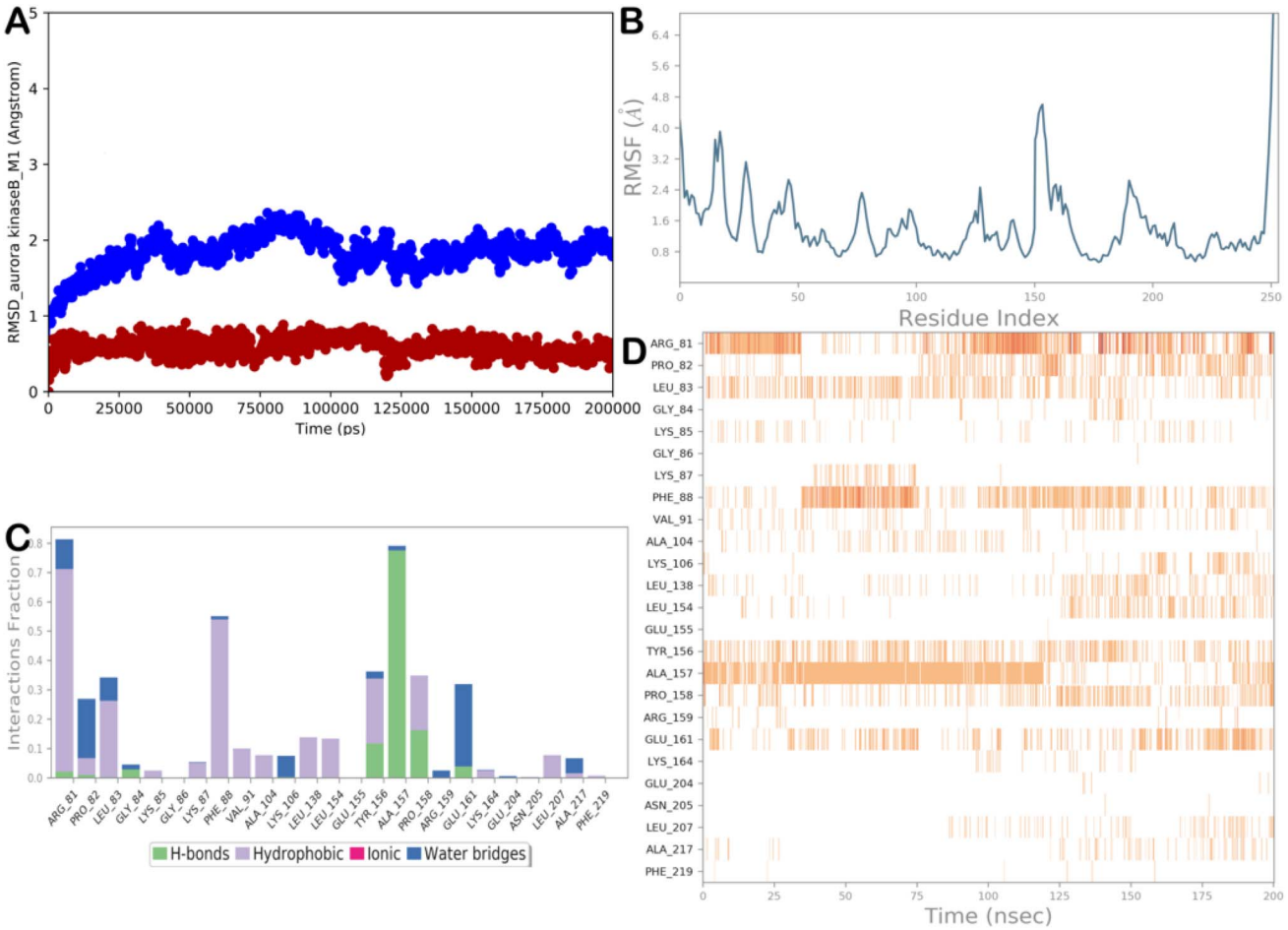

Fig. 15 (A) RMSD evaluation (protein: blue line; and ligand: red line). (B) RMSF assessment for the Aurora B/**M1**, obtained by docking studies, following a 200 ns molecular dynamics simulation. (C and D) **M1** observed throughout the molecular dynamics run. Four types of interactions can be distinguished: water bridges (blue), ionic (magenta), hydrophobic (grey), and H-bonds (green). Over the trajectory, the stacked bar charts are normalized. For instance, a value of 0.7 indicates that a particular contact is maintained 70% of the time during simulation. Values greater than 1.0 could occur because a protein residue could interact with the ligand more than once using the same subtype. A timeline explanation of the primary interactions is shown in the following diagram in the figure. Those residues that interact with the ligand in each trajectory frame are displayed in the output. A darker orange hue denotes several contacts that some residues have with the ligand. Maestro and Desmond software tools were utilized to generate the pictures (Maestro, Schrödinger LLC, release 2020-3).

compound displayed moderate lipophilicity, with an experimentally determined log *P* value of 1.63 ± 0.45, which remains within a range generally considered favorable for kinase inhibitors.[41] This balance suggests that, although aqueous solubility is limited, membrane permeability is likely adequate to support intracellular target engagement, potentially contributing to the observed cytotoxic activity. Collectively, these results indicate that future optimization should primarily focus on enhancing solubility through structural modification (*e.g.* salt formation) or formulation strategies while preserving the lipophilicity window required for effective dual VEGFR-2 and B-Raf inhibition.

3 Conclusion

This study successfully developed novel candidates of thienopyrimidine as dual Aurora B and VEGFR-2 inhibitors. Among the synthesized compounds, **M1** demonstrated the most promising pharmacological profile, demonstrating potent anticancer potential against different cancer cells, especially MCF-7 and MDA-MB-231 breast cancer cells, with activity comparable to Doxorubicin and superior to Sorafenib. **M1** showed potent enzymatic inhibition of Aurora B and VEGFR-2, supporting its dual kinase inhibitory potential at the biochemical level. Cellular studies revealed G1-phase arrest and enhanced apoptosis in MDA-MB-231 cells. *In vivo* evaluation in a DMBA-induced breast cancer model demonstrated marked tumor volume reduction with lower observed systemic toxicity compared to Doxorubicin. Histopathological and immunohistochemical analyses indicated reduced malignant features and enhanced apoptotic activity. Molecular docking and dynamic simulations suggested stable binding interactions within the active sites of both kinases.

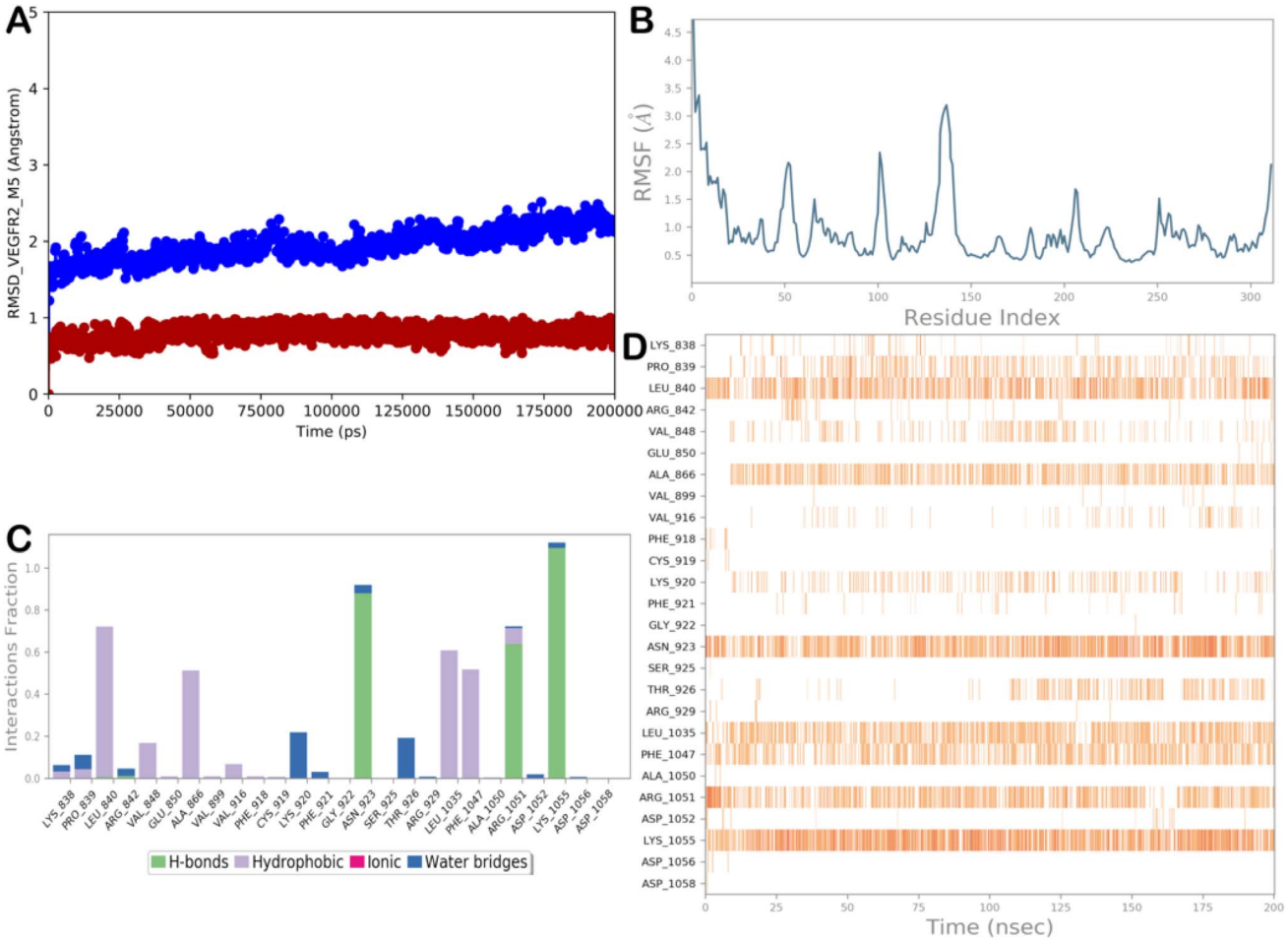

Fig. 16 (A) RMSD analysis (protein: blue line; and ligand: red line). (B) RMSF evaluation for the VEGFR-2/**M5**, derived from docking studies, after a 200 ns molecular dynamics simulation. (C and D) Visualization of compound **M5** during the molecular dynamics trajectory.

Overall, **M1** represents a promising dual enzymatic kinase inhibitor with significant anti-tutor potential. Further studies are warranted to confirm direct cellular target engagement and fully elucidate its molecular mechanism of action.

4 Experimental part

4.1. Chemistry

Melting points (uncorrected) were measured on a Stuart SMP 30. ^{1}H NMR (500 MHz) and ^{13}C NMR (125 MHz) spectra were recorded in DMSO-d_6 with TMS as internal standard at the NMR Laboratory, Faculty of Sciences, Mansoura University, Egypt. Chemical shifts (δ) are in ppm; peak notations used are s (singlet), d (doublet), t (triplet), m (multiplet), br (broad). Elemental analyses (C, H, N) were conducted at Cairo University, Egypt with a PerkinElmer 240; all results were within acceptable limits. Mass spectra were obtained from a Thermo Scientific GC/MS ISQ at the Regional Center for Mycology and Biotechnology, Al-Azhar University, Egypt. Reagents were sourced from Aldrich and other vendors. Reaction progress was monitored by TLC using Merck silica gel 60 F_{254} plates (hexane/ethyl acetate 1 : 1) and visualized under UV light at 245–366 nm. The key precursor compound **8** and the intermediate thiols **3a–e** were synthesized following reported procedures in literature.[31,34,38,40]

4.1.1. Synthetic methodology of the target thieno[2,3-*d*] pyrimidine-urea hybrids (M1–M5). A stirred solution of 4-chloro derivative **8** (0.001 mol) and potassium carbonate (0.0015 mol) in dry DMF (3 mL) was treated with the appropriate thiol intermediate **3a–e** (0.001 mol). The reaction was stirred for 12 h at ambient temperature. The reaction completion was observed by TLC. Upon completion, the mixture was poured into a cold water–ice mixture, promoting precipitation of the products. The resulting solids were separated by filtration, washed with cold water, and purified by recrystallization from ethanol, yielding the target compounds **M1–M5**.

*4.1.1.1. Ethyl 5-methyl-4-((5-(3-(p-tolyl)ureido)-1,3,4-thiadiazol-2-yl)thio)thieno[2,3-d] pyrimidine-6-carboxylate (**M1**).* ^{1}H NMR (500 MHz, DMSO-d_6) δ 9.63 (s, 1H, NH; D_2O exchangeable), 8.79 (s, 1H, pyrimidine-H), 7.52 (d, J = 8.2 Hz, 2H, Ph-H), 6.96 (d, J = 8.2 Hz, 2H, Ph-H), 4.34 (q, J = 7.1 Hz, 2H, OCH_2), 3.03 (s, 3H, CH_3), 2.17 (s, 3H, CH_3), 1.31 (t, J = 7.1 Hz, 3H, CH_3). ^{13}C NMR (126 MHz, DMSO-d_6) δ 166.21, 165.87, 161.85, 154.13, 154.04, 154.00, 138.99, 129.17, 129.00, 128.80, 128.12, 125.63, 117.71,

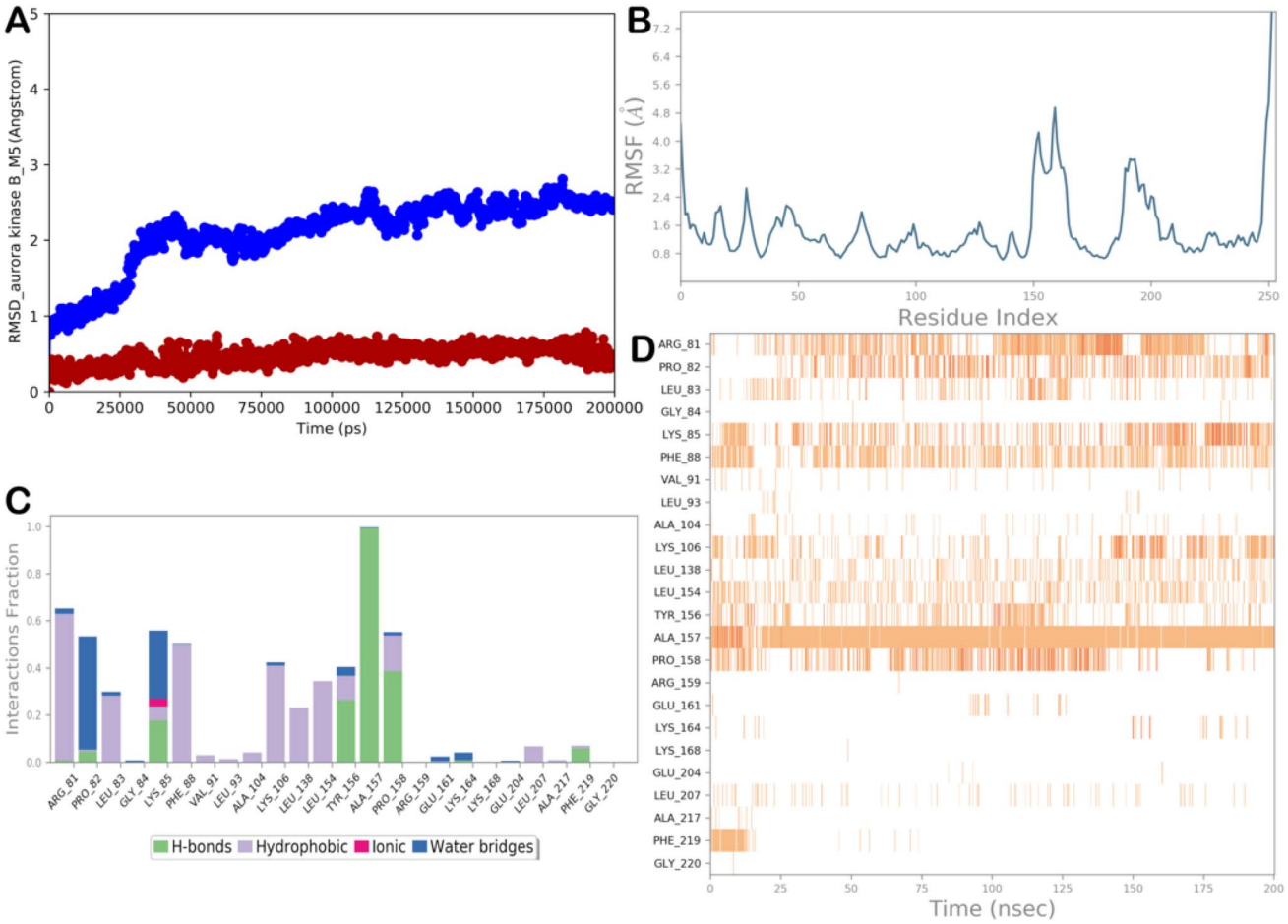

Fig. 17 (A) RMSD analysis (protein: blue line; and ligand: red line). (B) RMSF evaluation for the Aurora B/**M5**, derived from docking studies, after a 200 ns molecular dynamics simulation. (C and D) Visualization of compound **M5** during the molecular dynamics trajectory.

117.59, 61.91, 20.38, 16.21, 14.13. MS *m/z* (%): 487 (M^+). Anal. calcd for $C_{20}H_{18}N_6O_3S_3$ (%): C, 49.37; H, 3.73; N, 17.27. Found: C, 49.27; H, 3.75; N, 17.30.

*4.1.1.2. Ethyl 4-((5-(3-(4-methoxyphenyl)ureido)-1,3,4-thiadiazol-2-yl)thio)-5-methylthieno[2,3-d]pyrimidine-6-carboxylate (**M2**).* ^{1}H NMR (500 MHz, DMSO-d_6) δ 11.39 (s, 1H, NH; D_2O exchangeable), 9.23 (s, 1H, NH; D_2O exchangeable), 8.86 (s, 1H, pyrimidine-H), 7.39 (d, J = 8.6 Hz, 2H, Ph-H), 6.86 (d, J = 8.6 Hz, 2H, Ph-H), 4.32 (q, J = 7.1 Hz, 2H, OCH_2), 3.68 (s, 3H, OCH_3), 2.99 (s, 3H, CH_3), 1.29 (t, J = 7.1 Hz, 3H, CH_3). ^{13}C NMR (126 MHz, DMSO-d_6) δ 166.10, 162.59, 161.72, 159.21, 155.35, 153.81, 148.46, 138.62, 131.23, 128.07, 126.13, 120.84, 117.03, 114.08, 62.00, 55.21, 15.91, 14.07. MS *m/z* (%): 502 (M^+). Anal. calcd for $C_{20}H_{18}N_6O_4S_3$ (%): C, 47.80; H, 3.61; N, 16.72. Found: C, 47.85; H, 3.60; N, 16.68.

*4.1.1.3. Ethyl 4-((5-(3-(4-chloro-3-(trifluoromethyl)phenyl)ureido)-1,3,4-thiadiazol-2-yl)thio)-5-methylthieno[2,3-d]pyrimidine-6-carboxylate (**M3**).* ^{1}H NMR (500 MHz, DMSO-d_6) δ 12.43 (s, 1H, NH; D_2O exchangeable) 10.69 (s, 1H, NH; D_2O exchangeable), 8.83 (s, 1H, pyrimidine-H), 8.24 (d, J = 2.5 Hz, 1H, Ph-H), 7.83 (dd, J = 8.8, 2.5 Hz, 1H, Ph-H), 7.52 (d, J = 8.8 Hz, 1H, Ph-H), 4.32 (q, J = 7.1 Hz, 2H, OCH_2), 2.99 (s, 3H, CH_3), 1.30 (t, J = 7.1 Hz, 3H, CH_3). ^{13}C NMR (126 MHz, DMSO-d_6) δ 166.03, 163.92, 161.74, 154.98, 153.81, 139.42, 138.63, 131.93, 127.97, 126.81, 126.57, 126.03, 123.98, 123.09, 122.48, 121.81, 116.99, 61.97, 15.95, 14.08. MS *m/z* (%): 575 (M^+), 577 (M + 2). Anal. calcd for $C_{20}H_{14}ClF_3N_6O_3S_3$ (%): C, 41.78; H, 2.45; N, 14.62. Found: C, 42.00; H, 2.48; N, 14.60.

*4.1.1.4. Ethyl 4-((5-(3-(4-chlorophenyl)ureido)-1,3,4-thiadiazol-2-yl)thio)-5-methylthieno[2,3-d]pyrimidine-6-carboxylate (**M4**).* ^{1}H NMR (500 MHz, DMSO-d_6) δ 11.50 (s, 1H, NH; D_2O exchangeable), 9.65 (s, 1H, NH; D_2O exchangeable), 8.87 (s, 1H, pyrimidine-H), 7.50 (d, J = 8.8 Hz, 2H, Ph-H), 7.33 (d, J = 8.8 Hz, 2H, Ph-H), 4.32 (q, J = 7.1 Hz, 2H, OCH_2), 2.98 (s, 3H, CH_3), 1.30 (t, J = 7.1 Hz, 3H, CH_3). ^{13}C NMR (126 MHz, DMSO-d_6) δ 166.15, 164.22, 163.17, 161.74, 153.79, 147.53, 141.45, 138.60, 137.30, 128.88, 128.08, 126.85, 126.20, 120.50, 62.03, 15.91, 14.09. MS *m/z* (%): 507 (M^+), 509 (M + 2). Anal. calcd for $C_{19}H_{15}ClN_6O_3S_3$ (%): C, 45.01; H, 2.98; N, 16.58. Found: C, 45.08; H, 2.90; N, 16.61.

*4.1.1.5. Ethyl 4-((5-(3-(4-fluorophenyl)ureido)-1,3,4-thiadiazol-2-yl)thio)-5-methylthieno[2,3-d]pyrimidine-6-carboxylate (**M5**).* ^{1}H NMR (500 MHz, DMSO-d_6) δ 11.33 (s, 1H, NH; D_2O exchangeable), 9.19 (s, 1H, NH; D_2O exchangeable), 8.87 (s, 1H, pyrimidine-H), 7.47 (dd, J = 8.9, 4.9 Hz, 2H, Ph-H), 7.13 (t, J = 8.8 Hz, 2H, Ph-H), 4.32 (q, J = 7.1 Hz, 2H, OCH_2), 2.98 (s, 3H,

CH_3), 1.29 (t, $J = 7.1$ Hz, 3H, CH_3). ^{13}C NMR (126 MHz, DMSO-d_6) δ 166.10, 163.18, 161.67, 159.08, 157.17, 153.73, 138.52, 134.51, 128.02, 126.17, 121.04, 120.97, 115.60, 115.43, 61.97, 15.86, 14.04. MS m/z (%): 491 (M^+), 492 (M + 1). Anal. calcd for $C_{19}H_{15}FN_6O_3S_3$ (%): C, 46.52; H, 3.08; N, 17.13. Found: C, 46.47; H, 2.99; N, 17.20.

4.2. Biological evaluation

4.2.1. *In vitro* cytotoxicity (IC_{50}) screening. The cytotoxic potential of target compounds **M1–M5** was investigated against cancer cell lines including PC-3 (prostate), HeLa (cervical), HepG2 (liver), HCT-116 (colorectal), MCF-7 (hormone receptor-positive breast), and MDA-MB-231 (triple-negative breast), alongside WI-38 normal lung fibroblasts and MCF-10A mammary epithelial cells for selectivity assessment. All cell lines (ATCC) were cultured in RPMI-1640 supplemented with 10% fetal calf serum at 37 °C in 5% CO_2. Cells ($2.7–3.1 \times 10^4$ per well) were seeded into 96-well plates and allowed to adhere for 24 h. Compounds were dissolved in DMSO and applied as serial dilutions (0.1–300 μM). After 72 h treatment, cell viability was determined using MTT assay, with 20 μL MTT (5 mg mL^{-1}) added for 4 h. Formazan crystals were dissolved in DMSO : isopropanol (1 : 1) and absorbance measured at 590 nm. Cell viability was normalized to untreated controls and IC_{50} values calculated from dose–response curves. All experiments were conducted in triplicate, with three independent repeats.[42,43]

4.2.2. *In vitro* Aurora B and VEGFR-2 inhibition assay. The inhibitory activity of compounds **M1–M5** against Aurora B and VEGFR-2 kinases was assessed using luminescence-based assays with commercially available kinase assay kits (BPS Bioscience, USA), in accordance with the manufacturer's instructions. Serial dilutions of **M1–M5**, along with the reference inhibitors SP-96 (Aurora B) and Sorafenib (VEGFR-2), were prepared in the concentration range of 3–0.001 μM. Luminescence signals were recorded using a BioTek™ Synergy2 Microplate Reader (USA). Kinase activity in the absence of inhibitors was defined as 100%, and background (blank) values were subtracted from all measurements. The concentration of compound needed to decrease kinase activity by 50% (IC_{50}) was determined from dose–response curves using non-linear regression analysis.

4.2.3. Cell cycle distribution. MDA-MB-231 cells were exposed to compound **M1** at its IC_{50} concentration (5.37 μM) for 48 h. Post-treatment, cells were collected, washed with PBS, and fixed in 70% ethanol at 4 °C for 2 h. After centrifugation (800×*g*, 5 min, 4 °C), pellets were resuspended in PBS containing propidium iodide (PI) (0.02 mg mL^{-1}) and RNase A (0.1 mg mL^{-1}) (Elabscience Biotechnology, USA). Samples were incubated for 30 min at 37 °C in the dark, and DNA content was analyzed by flow cytometry using a Beckman Coulter Epics XL-MCL™ system. Cell cycle distribution (sub-G1, G1, S, and G2/M phases) was qualified with Flowing Software v2.5.1 (Turku Centre for Biotechnology, Finland).[43–45]

4.2.4. Apoptosis determination. Apoptotic effects were measured in MDA-MB-231 cells exposed to the IC_{50} concentration of test compound **M1** for 48 h. Cells were tainted with Annexin V-FITC and PI using an apoptosis detection kit (Elabscience Biotechnology, USA) and analyzed by flow cytometry. Data acquisition and quadrant-based quantification of viable, early apoptotic, late apoptotic, and necrotic populations were performed with ACEA NovoExpress™ software (ACEA Biosciences Inc., USA).[44,46]

4.2.5. *In vivo* anti-breast cancer activity assay of compound M1 and its effect on the apoptotic marker (caspase-3) level. The *in vivo* breast cancer study was conducted in compliance with ethical standards approved by the Research and Ethics Committee, Faculty of Pharmacy, Mansoura University, as well as by the Mansoura University Animal Care and Use Committee under approval code MU-ACUC (PHARM.R.25.08.56). The anti-tumor activity of compound **M1** was assessed according to established procedures reported in the literature.[47] Twenty 8-week-old Swiss albino female mice (20–25 g) were randomly assigned into five groups ($n = 5$/group): control, DMBA-induced, **M1**-treated (10 mg kg^{-1}, i.p.), DOX-treated (2 mg kg^{-1}, i.p.), and corresponding control. Breast cancer was induced by daily intraperitoneal administration of 7,12-dimethylbenz[*a*]anthracene for 20 days, with tumor volume and body weight monitored every five days.

At study end, animals were anesthetized and euthanized; breast tumors were collected, fixed in 10% neutral buffered formalin, and processed for histopathological (H&E) and immunohistochemical analysis of cleaved caspase-3. Sections were evaluated in a double-blinded manner, and morphometric analysis of apoptotic cells was performed on 18 high-power fields per section using IMAGE J/FIJI software. The detailed methodology is provided in the SI file.

5 Computational details

5.1. Ligands and protein preparation, and molecular docking

Compounds **M1** and **M5** were constructed using Maestro (Schrödinger LLC, 2020, v12.5) and energy-minimized in MacroModel (v12.9) with the OPLS3 force field and GB/SA solvent model without cutoff parameters. The PRCG minimization method was applied using a gradient convergence threshold of 0.001 and a maximum of 5000 iterations. LigPrep (v2.5) was then used to generate the most probable ionization states of the compounds at physiological pH (7.4 ± 0.2).[48–50] The crystal structures of hVEGFR-2 (PDB: 4ASD) and hAurora B (PDB: 4AF3) were collected from the Protein Data Bank, cleaned of crystallization components, and prepared using the Protein Preparation Wizard in Maestro, as previously detailed.[51,52] Molecular docking was performed using Glide (v8.8) in standard-precision mode, with energy grids centered on the co-crystallized ligands (scaling factor 1.0 Å, default parameters). Each compound was docked with 1000 poses subjected to post-docking minimization.[53–55]

5.2. Molecular dynamics methodology

Molecular dynamics (MD) simulations were performed with Desmond integrated into Maestro (Desmond Molecular

Dynamics System 6.4, D. E. Shaw Research, 2020; Maestro-Desmond Interoperability Tools, Schrödinger, 2020). The Desmond System Builder was used to prepare biological complexes by embedding them in an orthorhombic box containing TIP3P water molecules and Na^+/Cl^- ions to achieve a 0.15 M physiological salt concentration.[56,57] Simulations were conducted using the OPLS force field on two NVIDIA GPUs[48] *via* the CUDA API under the NPT ensemble (1.01325 bar, 300 K), employing the RESPA integrator,[58] Nose–Hoover thermostat,[59] and Martyna–Tobias–Klein method.[60] Long-range electrostatics were treated with the particle-mesh Ewald approach, while van der Waals and short-range electrostatics were truncated at 9.0 Å.[61] Each system underwent a multistep relaxation and equilibration cycle, followed by MD production runs. Post-simulation analysis was carried out using the Desmond analysis suite.

Ethical statement

The experimental design was approved by Mansoura University Animal Care and Use Committee (MU-ACUC) in accordance with ARRIVE guidelines for animal experimentation.

Conflicts of interest

The authors declare no conflicts of interest.

Data availability

The data supporting this study's findings are available from the corresponding author, A. H., upon reasonable request.

Supplementary information (SI) is available. See DOI: https://doi.org/10.1039/d5ra09370h.

Acknowledgements

The authors extend their appreciation to the Ongoing Research Funding Program (ORF-2026-1049), King Saud University, Riyadh, Saudi Arabia.

References

1 F. Bray, M. Laversanne, H. Sung, J. Ferlay, R. L. Siegel, I. Soerjomataram and A. Jemal, Global cancer statistics 2022: GLOBOCAN estimates of incidence and mortality worldwide for 36 cancers in 185 countries, *Ca-Cancer J. Clin.*, 2024, **74**, 229–263.

2 J. Kim, A. Harper, V. McCormack, H. Sung, N. Houssami, E. Morgan, M. Mutebi, G. Garvey, I. Soerjomataram and M. M. Fidler-Benaoudia, Global patterns and trends in breast cancer incidence and mortality across 185 countries, *Nat. Med.*, 2025, **31**, 1154–1162.

3 A. M. Karim, J. Eun Kwon, T. Ali, J. Jang, I. Ullah, Y.-G. Lee, D. W. Park, J. Park, J. W. Jeang and S. C. Kang, Triple-negative breast cancer: epidemiology, molecular mechanisms, and modern vaccine-based treatment strategies, *Biochem. Pharmacol.*, 2023, **212**, 115545.

4 N. M. Almansour, Triple-Negative Breast Cancer: A Brief Review About Epidemiology, Risk Factors, Signaling Pathways, Treatment and Role of Artificial Intelligence, *Front. Mol. Biosci.*, 2022, **9**, 836417.

5 A. Agelidis, A. Ter-Zakarian and M. Jaloudi, Triple-Negative Breast Cancer on the Rise: Breakthroughs and Beyond, *Breast Cancer*, 2025, **17**, 523–529.

6 Z. Chen, Y. Liu, M. Lyu, C. H. Chan, M. Sun, X. Yang, S. Qiao, Z. Chen, S. Yu, M. Ren, A. Lu, G. Zhang, F. Li and Y. Yu, Classifications of triple-negative breast cancer: insights and current therapeutic approaches, *Cell Biosci.*, 2025, **15**, 13.

7 J. M. Elkins, S. Santaguida, A. Musacchio and S. Knapp, Crystal Structure of Human Aurora B in Complex with INCENP and VX-680, *J. Med. Chem.*, 2012, **55**, 7841–7848.

8 M. M. Hasan, S. Tory, Y. K. Arslan, Y. Saygideger and Y. Tutar, Prognostic value of Aurora B expression in cancer patients: A meta-analysis, *Tumori J.*, 2025, **111**, 253–260.

9 P. Vats, C. Saini, B. Baweja, S. K. Srivastava, A. Kumar, A. S. Kushwah and R. Nema, Aurora kinases signaling in cancer: from molecular perception to targeted therapies, *Mol. Cancer*, 2025, **24**, 180.

10 S. Pellizzari, H. Athwal, A. C. Bonvissuto and A. Parsyan, Role of AURKB Inhibition in Reducing Proliferation and Enhancing Effects of Radiotherapy in Triple-Negative Breast Cancer, *Breast Cancer*, 2024, **16**, 341–346.

11 B. Ning, C. Liu, A. C. Kucukdagli, J. Zhang, H. Jing, Z. Zhou, Y. Zhang, Y. Dong, Y. Chen, H. Guo and J. Xu, Proteomic profiling identifies upregulation of aurora kinases causing resistance to taxane-type chemotherapy in triple negative breast cancer, *Sci. Rep.*, 2025, **15**, 3211.

12 C. P. Gully, F. Zhang, J. Chen, J. A. Yeung, G. Velazquez-Torres, E. Wang, S.-C. J. Yeung and M.-H. Lee, Antineoplastic effects of an Aurora B kinase inhibitor in breast cancer, *Mol. Cancer*, 2010, **9**, 42.

13 A. H. Kovacs, D. Zhao and J. Hou, Aurora B inhibitors as cancer therapeutics, *Molecules*, 2023, **28**, 3385.

14 R. W. Wilkinson, R. Odedra, S. P. Heaton, S. R. Wedge, N. J. Keen, C. Crafter, J. R. Foster, M. C. Brady, A. Bigley, E. Brown, K. F. Byth, N. C. Barrass, K. E. Mundt, K. M. Foote, N. M. Heron, F. H. Jung, A. A. Mortlock, F. T. Boyle and S. Green, AZD1152, a Selective Inhibitor of Aurora B Kinase, Inhibits Human Tumor Xenograft Growth by Inducing Apoptosis, *Clin. Cancer Res.*, 2007, **13**, 3682–3688.

15 F. Robert, H. Hurwitz, C. F. Verschraegen, R. Advani, C. Berman, P. Taverna and M. Evanchik, Phase 1 trial of SNS-314, a novel selective inhibitor of aurora kinases A, B, and C, in advanced solid tumor patients, *J. Clin. Oncol.*, 2008, **26**, 14642.

16 M. L. Maitland, S. Piha-Paul, G. Falchook, R. Kurzrock, L. Nguyen, L. Janisch, S. Karovic, M. McKee, E. Hoening, S. Wong, W. Munasinghe, J. Palma, C. Donawho, G. K. Lian, P. Ansell, M. J. Ratain and D. Hong, Clinical pharmacodynamic/exposure characterisation of the multikinase inhibitor ilorasertib (ABT-348) in a phase 1 dose-escalation trial, *Br. J. Cancer*, 2018, **118**, 1042–1050.

17 C. H. A. Cheung, W.-H. Lin, J. T.-A. Hsu, T.-C. Hour, T.-K. Yeh, S. Ko, T.-W. Lien, M. S. Coumar, J.-F. Liu and W.-Y. Lai, BPR1K653, a novel Aurora kinase inhibitor, exhibits potent anti-proliferative activity in MDR1 (P-gp170)-mediated multidrug-resistant cancer cells, *PLoS One*, 2011, **6**, e23485.

18 N. R. Lakkaniga, L. Zhang, B. Belachew, N. Gunaganti, B. Frett and H.-y. Li, Discovery of SP-96, the first non-ATP-competitive Aurora Kinase B inhibitor, for reduced myelosuppression, *Eur. J. Med. Chem.*, 2020, **203**, 112589.

19 R. Lugano, M. Ramachandran and A. Dimberg, Tumor angiogenesis: causes, consequences, challenges and opportunities, *Cell. Mol. Life Sci.*, 2020, **77**, 1745–1770.

20 B. P. Schneider and G. W. Sledge, Drug Insight: VEGF as a therapeutic target for breast cancer, *Nat. Clin. Pract. Oncol.*, 2007, **4**, 181–189.

21 S. Guo, L. S. Colbert, M. Fuller, Y. Zhang and R. R. Gonzalez-Perez, Vascular endothelial growth factor receptor-2 in breast cancer, *Biochim. Biophys. Acta, Rev. Cancer*, 2010, **1806**, 108–121.

22 X. Zhu and W. Zhou, The Emerging Regulation of VEGFR-2 in Triple-Negative Breast Cancer, *Front. Endocrinol.*, 2015, **6**, 159.

23 S. Nadar, M. Borkar and T. Khan, Thienopyrimidine: Unveiling the Versatile Potential of a Promising Heterocyclic Scaffold in Drug Discovery, *Chem. Biol. Drug Des.*, 2025, **105**, e70146.

24 P. Lagardère, C. Fersing, N. Masurier and V. Lisowski, Thienopyrimidine: A Promising Scaffold to Access Anti-Infective Agents, *Pharmaceuticals*, 2022, **15**, 35.

25 D. Zhao, A. H. Kovacs, M. Campbell, W. Floriano and J. Hou, Selective targeting of Aurora kinase B over A: Uncovering the structural basis for inhibitor specificity through molecular dynamics simulations, *J. Mol. Struct.*, 2023, **1292**, 136178.

26 A. Ghith, N. S. M. Ismail, K. Youssef and K. A. M. Abouzid, Medicinal Attributes of Thienopyrimidine Based Scaffold Targeting Tyrosine Kinases and Their Potential Anticancer Activities, *Arch. Pharm.*, 2017, **350**, 1700242.

27 E. Z. Elrazaz, R. A. T. Serya, N. S. M. Ismail, D. A. Abou El Ella and K. A. M. Abouzid, Thieno[2,3-d]pyrimidine based derivatives as kinase inhibitors and anticancer agents, *Future J. Pharm. Sci.*, 2015, **1**, 33–41.

28 W. J. McClellan, Y. Dai, C. Abad-Zapatero, D. H. Albert, J. J. Bouska, K. B. Glaser, T. J. Magoc, P. A. Marcotte, D. J. Osterling, K. D. Stewart, S. K. Davidsen and M. R. Michaelides, Discovery of potent and selective thienopyrimidine inhibitors of Aurora kinases, *Bioorg. Med. Chem. Lett.*, 2011, **21**, 5620–5624.

29 E. Z. Elrazaz, R. A. T. Serya, N. S. M. Ismail, A. Albohy, D. A. Abou El Ella and K. A. M. Abouzid, Discovery of potent thieno[2,3-d]pyrimidine VEGFR-2 inhibitors: Design, synthesis and enzyme inhibitory evaluation supported by molecular dynamics simulations, *Bioorg. Chem.*, 2021, **113**, 105019.

30 M. A. Farag, M. M. Kandeel, A. E. Kassab and S. I. Faggal, Medicinal attributes of thienopyrimidine scaffolds incorporating the aryl urea motif as potential anticancer candidates via VEGFR inhibition, *Arch. Pharm.*, 2024, **357**, 2400125.

31 A. Faraji, T. Oghabi Bakhshaiesh, Z. Hasanvand, R. Motahari, E. Nazeri, M. A. Boshagh, L. Firoozpour, H. Mehrabi, A. Khalaj, R. Esmaeili and A. Foroumadi, Design, synthesis and evaluation of novel thienopyrimidine-based agents bearing diaryl urea functionality as potential inhibitors of angiogenesis, *Eur. J. Med. Chem.*, 2021, **209**, 112942.

32 F. Sessa and F. Villa, Structure of Aurora B-INCENP in complex with barasertib reveals a potential transinhibitory mechanism, *Acta Crystallogr., Sect. F: Struct. Biol. Commun.*, 2014, **70**, 294–298.

33 A. Hamdi, H. W. El-Shafey, D. I. A. Othman, A. S. El-Azab, N. A. AlSaif and A. A. M. Abdel-Aziz, Design, synthesis, antitumor, and VEGFR-2 inhibition activities of novel 4-anilino-2-vinyl-quinazolines: Molecular modeling studies, *Bioorg. Chem.*, 2022, **122**, 105710.

34 M. M. Al-Sanea, A. Hamdi, A. A. B. Mohamed, H. W. El-Shafey, M. Moustafa, A. A. Elgazar, W. M. Eldehna, H. Ur Rahman, D. G. T. Parambi, R. M. Elbargisy, S. Selim, S. N. A. Bukhari, O. Magdy Hendawy and S. S. Tawfik, New benzothiazole hybrids as potential VEGFR-2 inhibitors: design, synthesis, anticancer evaluation, and in silico study, *J. Enzyme Inhib. Med. Chem.*, 2023, **38**, 2166036.

35 M. M. Al-Sanea, H. M. Hafez, A. A. Mohamed, H. W. El-Shafey, A. A. Elgazar, S. S. Tawfik, W. A. Ewes, S. Hussein, T. G. Alsahli and A. Hamdi, Design, Synthesis, Pharmacological Evaluation of Quinazolin-4 (3 H)-Ones Bearing Urea Functionality as Potential VEGFR-2 Inhibitors, *Drug Des., Dev. Ther.*, 2024, 5109–5127.

36 S. S. Tawfik, A. Hamdi, A. R. Ali, A. A. Elgazar, H. W. El-Shafey, A. S. El-Azab, A. H. Bakheit, M. M. Hefnawy, H. A. Ghabbour and A. A. M. Abdel-Aziz, S-Alkylated quinazolin-4(3H)-ones as dual EGFR/VEGFR-2 kinases inhibitors: design, synthesis, anticancer evaluation and docking study, *RSC Adv.*, 2024, **14**, 26325–26339.

37 M. McTigue, B. W. Murray, J. H. Chen, Y.-L. Deng, J. Solowiej and R. S. Kania, Molecular conformations, interactions, and properties associated with drug efficiency and clinical performance among VEGFR TK inhibitors, *Proc. Natl. Acad. Sci. U. S. A.*, 2012, **109**, 18281–18289.

38 W. A. Ewes, S. S. Tawfik, A. M. Almatary, M. Ahmad Bhat, H. W. El-Shafey, A. A. B. Mohamed, A. Haikal, M. A. El-Magd, A. A. Elgazar, M. Balaha and A. Hamdi, Identification of Benzothiazoles Bearing 1,3,4-Thiadiazole as Antiproliferative Hybrids Targeting VEGFR-2 and BRAF Kinase: Design, Synthesis, BIO Evaluation and In Silico Study, *Molecules*, 2024, **29**, 3186.

39 K. Wang, D. Kim and A. Dömling, Cyanoacetamide MCR (III): Three-Component Gewald Reactions Revisited, *J. Comb. Chem.*, 2010, **12**, 111–118.

40 S. Triloknadh, C. Venkata Rao, K. Nagaraju, N. Hari Krishna, C. Venkata Ramaiah, W. Rajendra, D. Trinath and Y. Suneetha, Design, synthesis, neuroprotective, antibacterial activities and docking studies of novel thieno

[2,3-d]pyrimidine-alkyne Mannich base and oxadiazole hybrids, *Bioorg. Med. Chem. Lett.*, 2018, **28**, 1663–1669.

41 R. Roskoski, Rule of five violations among the FDA-approved small molecule protein kinase inhibitors, *Pharmacol. Res.*, 2023, **191**, 106774.

42 H. S. Salam, M. M. Tawfik, M. R. Elnagar, H. A. Mohammed, M. A. Zarka and N. S. Awad, Potential Apoptotic Activities of Hylocereus undatus Peel and Pulp Extracts in MCF-7 and Caco-2 Cancer Cell Lines, *Plants*, 2022, **11**, 2192.

43 H. W. El-Shafey, M. M. Al-Sanea, M. R. Elnagar, A. M. Gendy, M. I. Serag, A. M. Almatary, M. A. Khalaf, M.-H. Abdulla, N. S. Alhassan, M.-A. V. Mohammed, W. M. Eldehna and A. Hamdi, Design and synthesis of novel 2-S-alkylated Quinazolinones as dual BRAFV600E and EGFR inhibitors in melanoma: Mechanistic insights from apoptosis and cell cycle modulation, *Bioorg. Chem.*, 2025, **161**, 108526.

44 M. M. F. Ismail, T. Z. Shawer, R. S. Ibrahim, M. R. Elnagar and Y. A. Ammar, New molecular hybrids integrated with quinoxaline and pyrazole structural motifs: VGFR2 inhibitors and apoptosis inducers, *Bioorg. Chem.*, 2025, **156**, 108182.

45 A. H. Abd El-Haleem, M. A. E.-K. Kassem, M. R. Elnagar, S. E. Abbas, A. M. El Kerdawy and A. K. Farouk, Furan-and furopyrimidine-based derivatives: Synthesis, VEGFR-2 inhibition, and in vitro cytotoxicity, *ACS Med. Chem. Lett.*, 2024, **15**, 2150–2157.

46 M. R. Abdelaal, E. Ibrahim, M. R. Elnagar, S. H. Soror and H. Haffez, Augmented Therapeutic Potential of EC-Synthetic Retinoids in Caco-2 Cancer Cells Using an In Vitro Approach, *Int. J. Mol. Sci.*, 2022, **23**, 9442.

47 M. A. Sabry, M. A. Ghaly, A. R. Maarouf and H. I. El-Subbagh, New thiazole-based derivatives as EGFR/HER2 and DHFR inhibitors: Synthesis, molecular modeling simulations and anticancer activity, *Eur. J. Med. Chem.*, 2022, **241**, 114661.

48 W. L. Jorgensen, D. S. Maxwell and J. Tirado-Rives, Development and Testing of the OPLS All-Atom Force Field on Conformational Energetics and Properties of Organic Liquids, *J. Am. Chem. Soc.*, 1996, **118**, 11225–11236.

49 A. P. Saraswati, N. Relitti, M. Brindisi, J. D. Osko, G. Chemi, S. Federico, A. Grillo, S. Brogi, N. H. McCabe, R. C. Turkington, O. Ibrahim, J. O'Sullivan, S. Lamponi, M. Ghanim, V. P. Kelly, D. Zisterer, R. Amet, P. Hannon Barroeta, F. Vanni, C. Ulivieri, D. Herp, F. Sarno, A. Di Costanzo, F. Saccoccia, G. Ruberti, M. Jung, L. Altucci, S. Gemma, S. Butini, D. W. Christianson and G. Campiani, Spiroindoline-Capped Selective HDAC6 Inhibitors: Design, Synthesis, Structural Analysis, and Biological Evaluation, *ACS Med. Chem. Lett.*, 2020, **11**, 2268–2276.

50 M. Brindisi, C. Ulivieri, G. Alfano, S. Gemma, F. de Asís Balaguer, T. Khan, A. Grillo, G. Chemi, G. Menchon, A. E. Prota, N. Olieric, D. Lucena-Agell, I. Barasoain, J. F. Diaz, A. Nebbioso, M. Conte, L. Lopresti, S. Magnano, R. Amet, P. Kinsella, D. M. Zisterer, O. Ibrahim, J. O'Sullivan, L. Morbidelli, R. Spaccapelo, C. Baldari, S. Butini, E. Novellino, G. Campiani, L. Altucci, M. O. Steinmetz and S. Brogi, Structure-activity relationships, biological evaluation and structural studies of novel pyrrolonaphthoxazepines as antitumor agents, *Eur. J. Med. Chem.*, 2019, **162**, 290–320.

51 E. R. da Silva, S. Brogi, J. F. Lucon-Júnior, G. Campiani, S. Gemma and C. d. C. Maquiaveli, Dietary polyphenols rutin, taxifolin and quercetin related compounds target Leishmania amazonensis arginase, *Food Funct.*, 2019, **10**, 3172–3180.

52 S. Brogi, A. Fiorillo, G. Chemi, S. Butini, M. Lalle, A. Ilari, S. Gemma and G. Campiani, Structural characterization of Giardia duodenalis thioredoxin reductase (gTrxR) and computational analysis of its interaction with NBDHEX, *Eur. J. Med. Chem.*, 2017, **135**, 479–490.

53 R. A. Friesner, J. L. Banks, R. B. Murphy, T. A. Halgren, J. J. Klicic, D. T. Mainz, M. P. Repasky, E. H. Knoll, M. Shelley, J. K. Perry, D. E. Shaw, P. Francis and P. S. Shenkin, Glide: A New Approach for Rapid, Accurate Docking and Scoring. 1. Method and Assessment of Docking Accuracy, *J. Med. Chem.*, 2004, **47**, 1739–1749.

54 M. Paolino, M. Brindisi, A. Vallone, S. Butini, G. Campiani, C. Nannicini, G. Giuliani, M. Anzini, S. Lamponi, G. Giorgi, D. Sbardella, D. M. Ferraris, S. Marini, M. Coletta, I. Palucci, M. Minerva, G. Delogu, I. Pepponi, D. Goletti, A. Cappelli, S. Gemma and S. Brogi, Development of Potent Inhibitors of the Mycobacterium tuberculosis Virulence Factor Zmp1 and Evaluation of Their Effect on Mycobacterial Survival inside Macrophages, *ChemMedChem*, 2018, **13**, 422–430.

55 A. Vallone, S. D'Alessandro, S. Brogi, M. Brindisi, G. Chemi, G. Alfano, S. Lamponi, S. G. Lee, J. M. Jez, K. J. M. Koolen, K. J. Dechering, S. Saponara, F. Fusi, B. Gorelli, D. Taramelli, S. Parapini, R. Caldelari, G. Campiani, S. Gemma and S. Butini, Antimalarial agents against both sexual and asexual parasites stages: structure-activity relationships and biological studies of the Malaria Box compound 1-[5-(4-bromo-2-chlorophenyl)furan-2-yl]-N-[(piperidin-4-yl)methyl]methanamine (MMV019918) and analogues, *Eur. J. Med. Chem.*, 2018, **150**, 698–718.

56 H. Sirous, G. Chemi, S. Gemma, S. Butini, Z. Debyser, F. Christ, L. Saghaie, S. Brogi, A. Fassihi, G. Campiani and M. Brindisi, Identification of Novel 3-Hydroxy-pyran-4-One Derivatives as Potent HIV-1 Integrase Inhibitors Using in silico Structure-Based Combinatorial Library Design Approach, *Front. Chem.*, 2019, **7**, 574.

57 W. L. Jorgensen, J. Chandrasekhar, J. D. Madura, R. W. Impey and M. L. Klein, Comparison of simple potential functions for simulating liquid water, *J. Chem. Phys.*, 1983, **79**, 926–935.

58 D. D. Humphreys, R. A. Friesner and B. J. Berne, A Multiple-Time-Step Molecular Dynamics Algorithm for Macromolecules, *J. Phys. Chem.*, 1994, **98**, 6885–6892.

59 W. G. Hoover, Canonical dynamics: Equilibrium phase-space distributions, *Phys. Rev. A*, 1985, **31**, 1695–1697.

60 G. J. Martyna and D. J. Tobias, Constant pressure molecular dynamics algorithms, *J. Chern. Phys.*, 1994, **5**, 101.

61 U. Essmann, L. Perera, M. L. Berkowitz, T. Darden, H. Lee and L. G. Pedersen, A smooth particle mesh Ewald method, *J. Chem. Phys.*, 1995, **103**, 8577–8593.